Two-phase natural circulation and flow boiling with seawater

by

Daniel Franken

B.S., Kansas State University, 2017

A THESIS

submitted in partial fulfillment of the
requirements for the degree

MASTER OF SCIENCE

Department of Mechanical and Nuclear Engineering
College of Engineering

KANSAS STATE UNIVERSITY
Manhattan, Kansas

2019

Approved by:

Major Professor
Hitesh Bindra

Copyright

© Daniel Franken 2019.

Abstract

Two-phase natural circulation experiments were performed with artificial seawater as a working fluid. The experimental work performed in this investigation is focused on understanding the role of dissolved salts in the water on steady-state two-phase natural circulation flow rate characteristics. Experiments were performed measuring mass flow rates on a natural circulation loop with three process fluids, artificial seawater, tap water, and deionized water. The flow characteristics of each fluid were captured at the same heat flux and pressure condition to measure differences in mass flow rate and hydrodynamic conditions. The time-averaged mass flow rates under a quasi-steady state condition were found to be very similar under the same heat flux conditions for each fluid. Artificial seawater showed to be more stable compared to the other two fluids at higher heat flux. Instrumentation measurements recorded at approximately a 2-second interval showed that mass flow oscillations were significantly higher in the cases of the tap water and deionized water. The use of a high-speed camera showed that the bubble departure diameters were much smaller for the artificial seawater case compared to the other cases. The smaller departure diameters were partly attributed to the increase in local wettability caused by the scale formation during boiling. Another explanation to the smaller departure diameters is the local increase in salt concentration around the bubble, which increased local boiling point and reduced bubble growth time. The use of a visually transparent riser section revealed that the artificial seawater inhibited bubble coalescence and resulted in a bubbly flow regime for the range of heat fluxes tested. The observations in characteristic flow changes explained the reduced pressure drop across the test section when artificial seawater was used.

Table of Contents

List of Figures vi

List of Tables vii

Acknowledgements viii

Nomenclature ix

1 Introduction 1

2 Background and Literature Review 3

2.1 Seawater and Fresh water: Differences in the properties 3

2.1.1 Hydrodynamic differences 3

2.1.2 Thermodynamic differences 6

2.2 Bubble Growth and Departure review 10

2.3 Electrolyte boiling review 15

2.4 Natural circulation review 16

2.5 Flow Patterns 18

2.6 Pressure Drop 21

2.6.1 Homogeneous Flow Model 22

2.6.2 Separated Flow Models 24

2.7 Void Fractions 27

2.7.1 Homogeneous Flow 28

2.7.2 Separated Flow 28

3 Experimental setup and operation . . . 29
3.1 Setup . . . 29
3.1.1 Heater . . . 29
3.1.2 Heat Exchanger . . . 30
3.1.3 Test Section . . . 31
3.1.4 Valves and Flow Channel . . . 31
3.1.5 Measurement Devices . . . 31
3.2 Operation . . . 32

4 Results and Discussion . . . 35
4.1 Mass Flow Oscillations . . . 35
4.2 Monitoring dissolved salts . . . 37
4.3 Bubble Dynamics . . . 39
4.4 Pressure Drop . . . 41

5 Conclusions and Future Work . . . 45

Bibliography . . . 47

A Experimental Setup . . . 53

B MATLAB Code . . . 55

List of Figures

2.1 Density ratio with temperature at 200 kPa (absolute) 4

2.2 Viscosity ratio with temperature at 200 kPa (absolute) 5

2.3 Thermodynamic quality difference between seawater and fresh water 8

2.4 Void fraction difference between seawater and fresh water 9

2.5 Stages of bubble growth 11

2.6 Orientation of natural circulation loop 17

2.7 Flow patterns in upward vertical co-current flow 19

2.8 Flow pattern development in heated vertical pipe 21

2.9 Comparison of two-phase multipliers, properties taken at 101.325 kPa 27

3.1 Experimental setup 30

3.2 Pressure and temperature at steady state conditions 33

4.1 Mass flow rate versus heater power at varying salt concentrations 36

4.2 Mass flow oscillations versus heater power at varying salt concentrations . . 37

4.3 Electrical conductivity with time 38

4.4 Bubble formation at heater surface 40

4.5 Distribution of salt at bubble liquid-vapor interface 41

4.6 Bubble formation in riser section 42

4.7 Pressure drop over test section with heater power 43

A.1 Experimental setup 54

List of Tables

2.1 Seawater and deionized water properties at 60°C and atmospheric pressure . 4

2.2 Various thermodynamic properties 6

2.3 Cation and Anion major constituents[1] 13

3.1 Instrumentation error 32

3.2 Cation and Anion concentration comparison of major constituents[1] 32

4.1 Dissolved solids by electrical conductivity 38

Acknowledgments

I would like to thank Dr. Bindra for all his help and guidance in my research as an undergraduate and graduate student. I was very fortunate to work for Dr. Bindra on his two phase natural circulation project as it allowed me to experience aspects of analysis and engineering which I had not previously had.

I also would like to thank Dr. Steven Eckels and Dr. Mingjun Wei for the time and for being apart of my thesis committee. I would also like to thank Dan Gould, Zayed Ahmed, Seth Eckels, and Brendan Ward for their helpful ideas and suggestions. And of course, I don't know how I would have completed my work without the support of my lovely wife, Ellen.

Further, I thank the Department of Energy Nuclear Energy University Program Graduate Fellowship for their support of my graduate research.

Nomenclature

α	Void fraction
Δp	Pressure drop $[Pa]$
ΔT	Change in temperature $[°C]$
$\dot{m}$	Mass flow rate $[kg/s]$
$\frac{dp}{dz}$	Pressure drop gradient $[N/m^3]$
μ	Dynamic viscosity $[Pa \cdot s]$
μ_{tp}	Two-phase dynamic viscosity $[Pa \cdot s]$
Φ_{tp}	Two-phase multiplier
ρ	Density $[kg/m^3]$
σ	Surface tension $[N/m]$
A	Area $[m^2]$
C_p	Specific heat capacity $[kJ/kg \cdot K]$
D	Diameter $[m]$
f_{tp}	Two-phase frictional pressure drop
G	Mass flux $[kg/m^2 s]$
g	Acceleration due to gravity $[m/s^2]$
h	Enthalpy $[kJ/kg]$

h_{lv} Latent heat of vaporization $[kJ/kg]$

$Ja = C_p \Delta T / h_{lv}$ Jakob Number

L Length $[m]$

P Pressure $[Pa]$

Q Power $[W]$

R Radius $[m]$

$Re = \frac{GD}{\mu_{tp}}$ Reynolds number

V Volume $[m^e]$

x Vapor quality

Chapter 1

Introduction

Two-phase natural circulation is a flow process which has been used for decades in many different industrial processes. The most notable processes include passive safety systems in nuclear reactors, electronic cooling, solar water heaters, geothermal systems, heat exchangers, desalination, and refrigeration systems. The reason for the common use of two-phase flow is due to the high heat transfer capabilities which occur due to boiling. A variety of fluids have been investigated in two-phase flow for various applications, the most common investigations being with commercial refrigerants and distilled water. With the ever-growing demand for access to clean water sources, there has been an increased investigation into using seawater as a process fluid. Possible applications of the study of two-phase flow with dissolve salt impurities involve and emergency injection systems for nuclear reactor safety. Seawater is often used as heat transfer fluid for industrial processes given its relative cost, which is usually lower than freshwater. One common area for the use of seawater is in power plants, where the seawater is used as a heat sink and coolant for the working fluid of the plant. Other areas include boilers and process heaters for other chemical industrial processes.

The Fukushima-Daiichi Nuclear Power Plant (NPP) accident of 2011 introduced the nuclear community to an unfamiliar problem. The accident involved the tripping of the reactor and an immediate shutdown following a magnitude 9.0 earthquake off the coast of Japan. Backup generators were used to cool the reactor core after shutdown; however, they

were disabled after a tsunami overcame the protective seawall of the plant and flooded the generators housing. This led to the eventual explosion and the need for replacement of cooling water. In an attempt to keep the reactor cooled, seawater was pumped into the system. The effect of injection seawater was not yet known. One concern was that as the core boils the seawater, the dissolved salts would then deposit on the surface of the heater. Typically salts have low thermal conductivity and would, therefore, decrease the heat transfer rate from the core to the water. The decreased heat transfer rates mean that the fuel temperature would increase as further boiling takes place. Eventually, the fuel rods reached a critical temperature in which they were structurally unstable and eventually melted. Upon melting the fuel, rods settled at the bottom of the reactor chamber similar to a debris bed. It was unknown at the time how the seawater would influence the hydrodynamics of the natural circulation and the effect of the salts on the heat transfer rates. As most NPPs are located next to large bodies of water, typically emergency injection of raw water from the large water body is considered the ultimate long term safety system.

The next chapter will focus on a review of the characteristic differences between freshwater and seawater as well as two-phase flow characteristics. In Chapter 3, the experiment and characteristics components are discussed in detail. Chapter 4 provides the experimental results and a discussion of why those results were found.

Chapter 2

Background and Literature Review

This background is meant to provide critical information for understanding the major differences and flow effects that may occur due to the inclusion of dissolved salts in water. The review begins with the relative differences between seawater and fresh water as it relates to the hydrodynamic properties. These crucial characteristics will determine how the flow behaves and what mass flow rates and two-phase flow regimes are present. Then thermal properties will be discussed as to how it will effect the production of vapor in a two-phase flow system. Next, the inclusion of salts will be investigated in how it will impact the heated surface, and thermal boundary effects will drive nucleation at the heater's surface. The remainder of the chapter will focus on background on two-phase flow regimes and associated dynamics.

2.1 Seawater and Fresh water: Differences in the properties

2.1.1 Hydrodynamic differences

The differences in the hydrodynamic properties of seawater and distilled water are listed in Table 2.1. These values are important to compare as the hydrodynamics will determine

Table 2.1: *Seawater and deionized water properties at 60° C and atmospheric pressure*

Property	Seawater[2;3]	Deionized[4]	Ratios
Density [kg/m^3]	1008.9	983.3	1.026
Dynamic Viscosity [Pa·s]	5.07E-4	4.67E-4	1.089
Surface Tension [mN/m]	67.44	66.24	1.018
Kinematic Viscosity [m^2/s]	5.04E-7	4.74E-7	1.063

many of the characteristic flow behaviors. The influence of the hydrodynamic properties can be seen in pressure drop, bubble behavior, and flow stability. The properties for seawater were taken as a pure mixture, where the values of the salts and pure water were averaged to get the values on a per mass basis.

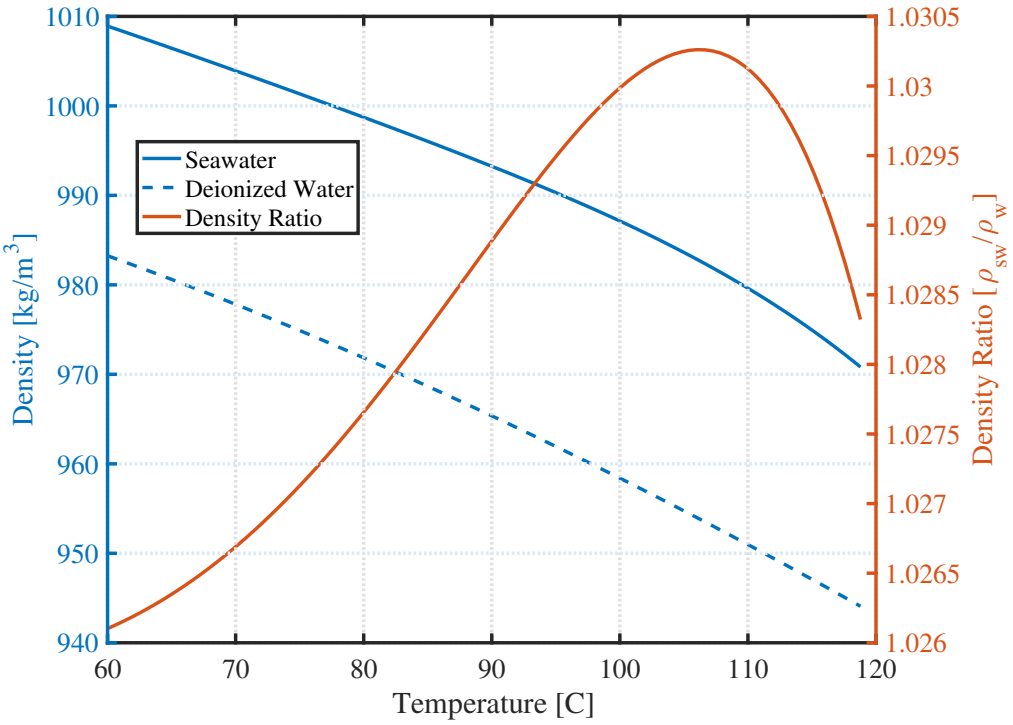


Figure 2.1: *Density ratio with temperature at 200 kPa (absolute)*

One of the critical difference to note is that the density of seawater is higher than the density of freshwater. Since fluid density directly affects body forces and pressure drop,

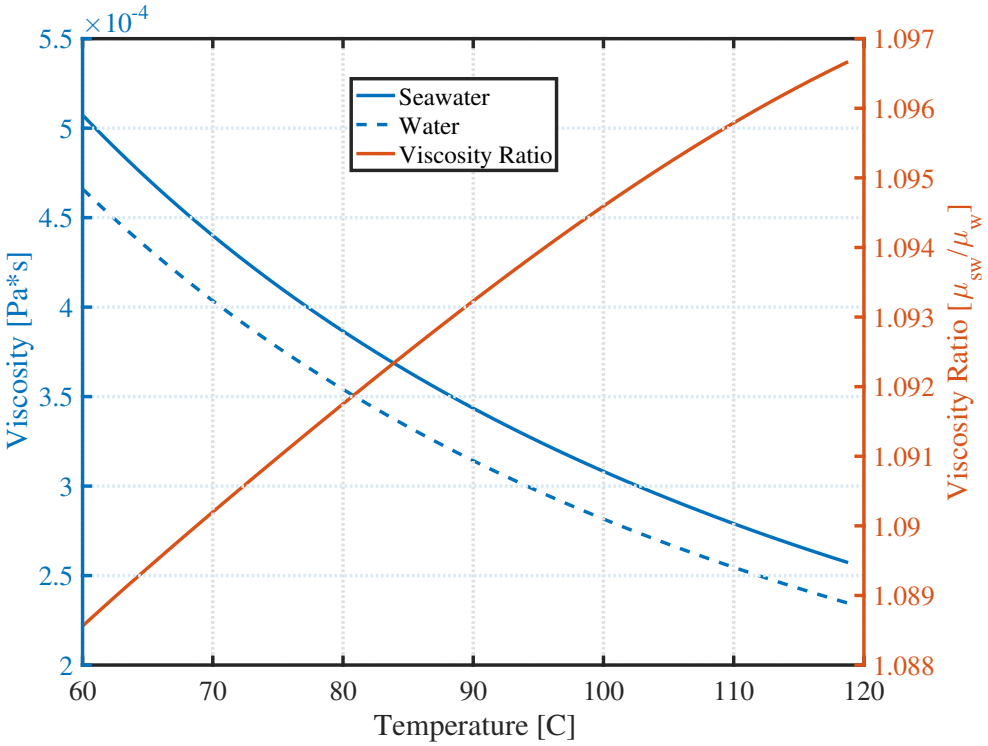


Figure 2.2: *Viscosity ratio with temperature at 200 kPa (absolute)*

changes in density will impact the hydrodynamic characteristics of natural circulation. An increased density will lead to a higher static pressure drop under the same void conditions under two-phase flow. Additionally, the increase in dynamic viscosity in seawater will lead to an increase in frictional pressure drop. The dynamic viscosity also plays a role in the coalesce of bubbles under a flow boiling scenario. Lessard and Zieminski[5] found that bubbles in electrolyte solutions tend to coalesce when the relative viscosity was less than 1.03 compared to water and greatly inhibited when it was higher than 1.07, as is the case for seawater shown in Table 2.1. The results presented by Lessard and Zieminski are only relevant to solutions which only contain water and dissolved salts. Further, the higher surface tension of seawater would cause an expected production of larger bubbles following the Laplace pressure Equation 2.1. This is assuming all other variables included in bubble growth are kept constant between seawater and freshwater, this is obviously an incorrect assumption, but it gives the idea of how surface tension alone impacts bubble size.

Table 2.2: *Various thermodynamic properties*

Property	Seawater[2;3]	Deionized Water[4]	Ratios
Latent Heat of Vaporization [kJ/kg]	2122.9	2201.6	0.964
Inlet Enthalpy [kJ/kg]	240.1	251.3	0.956
Saturation Enthalpy [kJ/kg]	484.6	504.4	0.961
Specific Heat Capacity @ 60°C [kJ/kgK]	4.014	4.183	0.960
Thermal Conductivity @ Saturation [W/mK]	0.681	0.682	0.999
Boiling Point Elevation [°C]	0.585	N/A	N/A

$$P_{inside} - P_{outside} = \frac{2\sigma}{R} \tag{2.1}$$

Where R is the radius of the bubble, and σ is the surface tension. The left-hand side of the equation refers to the pressure inside and outside of the bubble.

2.1.2 Thermodynamic differences

Another critical factor in the flow characteristics of two-phase flow is the thermodynamic properties of the fluid. The thermodynamic properties will influence the amount of vapor generation, saturation temperature, wall superheat, and other temperature-related properties. A table of a few reference properties are in Table 2.2. The inlet enthalpy was taken at a temperature of 60°C, while the saturation enthalpy was taken at 120.2°C, which is the saturation temperature of deionized water at 200 kPa absolute. As mentioned previously, the properties from the tables are taken as a mixture average on a per mass basis.

A vital difference between the two fluids is the enthalpy and latent heat of vaporiza-

tion values. The inlet enthalpy and saturation enthalpy values for seawater are lower than for deionized water. Additionally, the difference between the inlet enthalpy and saturation enthalpy values are lower for seawater than they are for deionized water. This difference indicates that seawater would reach a saturation condition at a lower heat input value than deionized water. The lower saturation enthalpy and latent heat of vaporization for the seawater case would lead to an increase in vapor generation when compared to deionized water. However, this is misleading as the values for enthalpy, and latent heat of vaporization are taken on a per unit mass basis. The dissolved salts present in the seawater would effectively reduce the amount of water present per unit of mass of seawater. Due to density differences, if both seawater and deionized water had the same mass flow rate, the actual amount of water flowing would be lower in the seawater case. The effective changes in properties can be seen by looking at the energy balance of the system, assuming no environmental losses. The energy balance equation is the following:

$$\dot{Q} = \dot{m}_{lv} h_{lv} + \dot{m}_{tot} C_p \Delta T \tag{2.2}$$

Where the right side term describes the sensible heating, and the left side term is for the latent heating. The $\dot{Q}$ represents the power added to the system. The $\dot{m}_{lv}$ represents the vapor generation rate. By dividing both sides of the equation by the latent heat of vaporization, the Jakob number can be incorporated into the equation.

$$\frac{\dot{Q}}{h_{lv}} = \dot{m}_{lv} + \dot{m}_{tot} Ja \tag{2.3}$$

By looking at Table 2.2, it can be seen that the Jakob number for each fluid case would be approximately the same. For the seawater case, the ΔT term is larger than for deionized water due to the boiling point elevation. Further, the latent heat of vaporization is lower for seawater, increasing both sides of the equation. The smaller specific heat capacity of seawater would lower the value of the Jakob number. The changes in latent heat, specific heat capacity, and boiling point elevation make it difficult to determine the exact impact

of the changes on the vapor quality. The differences in thermodynamic properties may be offset by the density differences and would make determining vapor quality difficult. Under a lower pressure condition, any small differences in vapor quality would have a significant impact on the void fraction and pressure drop. The following equation describes an enthalpy approach to a quality calculation, where x is the vapor quality[6].

$$x = \frac{\Delta h_{gain} + h_{in} - h_{sat}}{h_{lv}} \tag{2.4}$$

Where Δh_{gain} can be described by the following:

$$\Delta h_{gain} = \frac{\dot{Q}}{\dot{m}_{tot}} \tag{2.5}$$

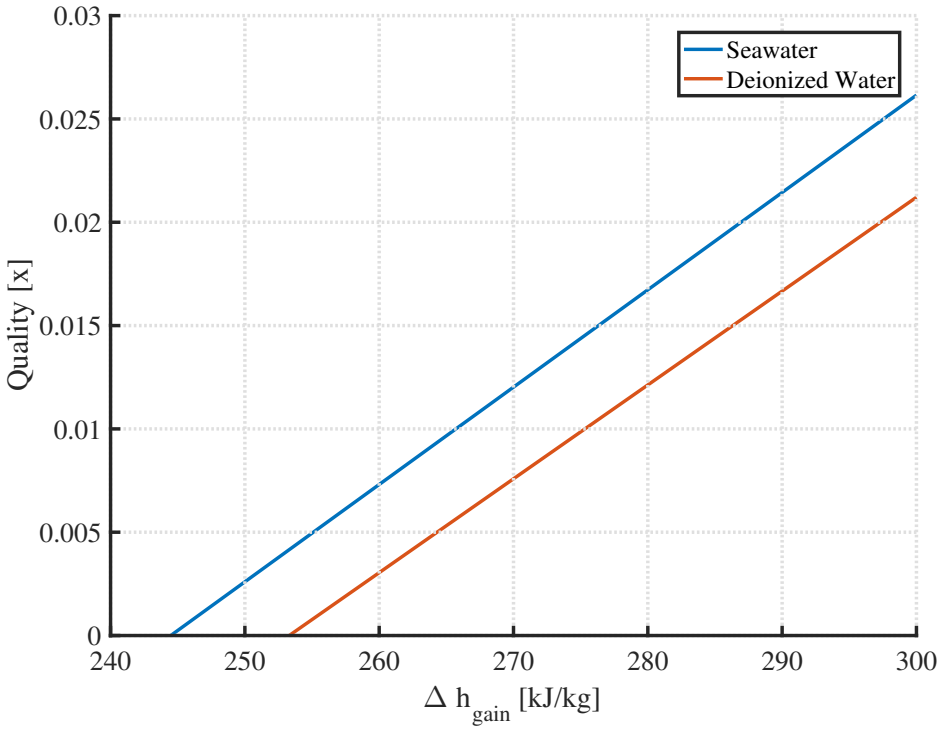


Figure 2.3: *Thermodynamic quality difference between seawater and fresh water*

By looking at the above Equations 2.4 and 2.5 an enthalpy approach to a quality calculation can be seen. If both the seawater and freshwater cases have the same mass flow rates at equivalent heater powers, then the enthalpy gain will be the same in both the sea-

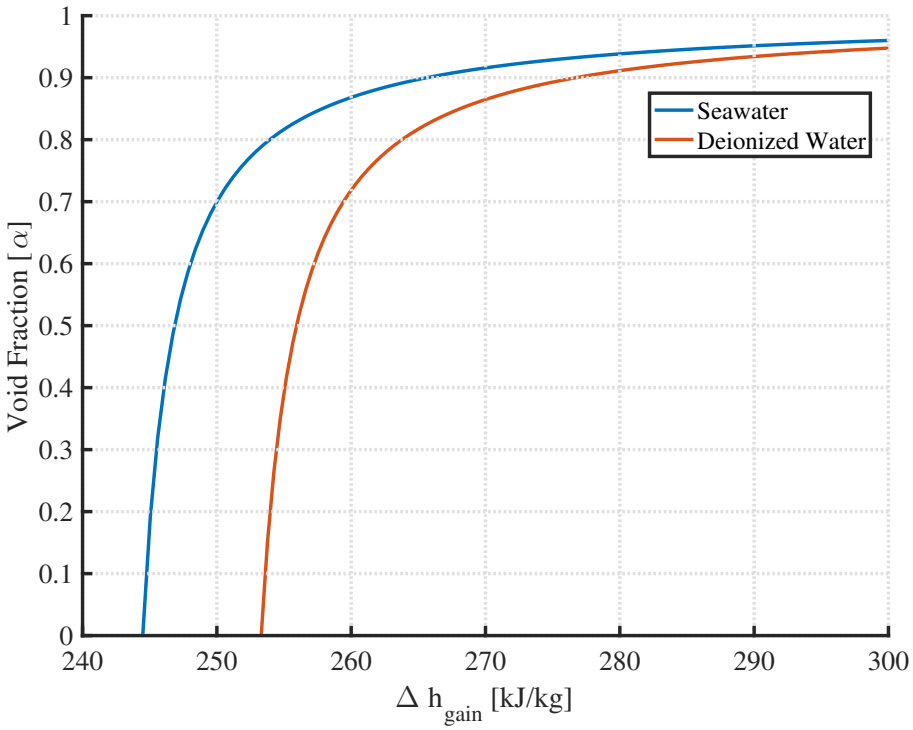


Figure 2.4: *Void fraction difference between seawater and fresh water*

water and freshwater cases. It is uncertain if there would be any noticeable difference in quality between the fluids. The seawater case has a smaller difference between inlet and saturation enthalpy for seawater, but a lower heat of vaporization, therefore, making quality calculations difficult. Again, though this cannot be verified as the decrease in latent heat of vaporization and enthalpy difference between inlet and saturation conditions are offset by the lower amount of water per unit mass of seawater. Following the mixture properties of seawater purely and deionized water, the expected quality, and void fractions are shown in Figures 2.3 and 2.4. Figure 2.3 shows the thermodynamic vapor equilibrium for the different water cases with water entering the heated section at a temperature of 60 °C and pressure of 6.895 kPa absolute. Figure 2.4 shows the discrepancy in void fraction produced by the small differences in quality. It should be noted that the thermodynamic equilibrium qualities are not what would be seen in the actual experiment. Due to subcooled boiling, there would be some vapor generated before a thermodynamic equilibrium condition has been met. Further, the differences shown in the void fraction are expected to be smaller in a real-world scenario

as the impacts of the dissolved salts may reduce the overall vapor generation. During boiling at the heater's surface, it is expected that there is a supersaturated condition as dissolved salts accumulate near the surface. This supersaturated condition would increase the boiling point temperature and therefore, the required enthalpy to reach saturation enthalpy. Additionally, as the dissolved salts begin to deposit on the surface, the heating will become less efficient and produce less vapor. These factors will shift the quality and void fraction curve of seawater shown in Figure 2.3 and 2.4 to the right.

The potential increase in vapor generation would have a significant effect on the static pressure drop, and the frictional pressure drop developed in the system. Another difference is the boiling point elevation, which is only a value of 0.585 °C. The boiling point elevation is expected to be higher on the surface of the heater as the generation of bubbles would create a supersaturated condition for the dissolved solids at the surface. The increased concentration of the dissolved salts at the surface of the heater would lead to an even higher boiling point elevation. Determining the exact increase in boiling point elevation due to supersaturation is challenging and will not be explored here. The thermal conductivity values are approximately the same and would not play a significant role in any flow differences seen between the two fluids.

2.2 Bubble Growth and Departure review

The driving force in two-phase natural circulation loops is due to the density differences between the legs of the loop. This density difference is mostly impacted by bubble growth, and it has been shown in previous literature that the presence of dissolved salts primarily alters the behavior of bubble growth dynamics compared to fresh water. Dissolved salts mainly alter bubble growth through changes in bubble coalescence and the number of active nucleation sites. Phase change for a pure liquid into a vapor can occur through two main thermodynamic processes, cavitation, and boiling. The former occurs when the pressure experienced by the liquid falls below the vapor pressure, and nucleation occurs. The latter is when the temperature of the liquid exceeds the saturation temperature of the liquid, and

nucleation occurs.

Bubble nucleation and growth is a complicated process which is still heavily investigated. Many literature reports revolve around the bubble growth seen in pool boiling experiments. Flow boiling bubble nucleation and growth is different from pool boiling but shares some similar characteristics. Part of the complexity lies with the highly turbulent conditions which take place during the boiling process. Other variables which influence bubble growth are wall temperature, boiling point, surface roughness, liquid properties, and several other factors.

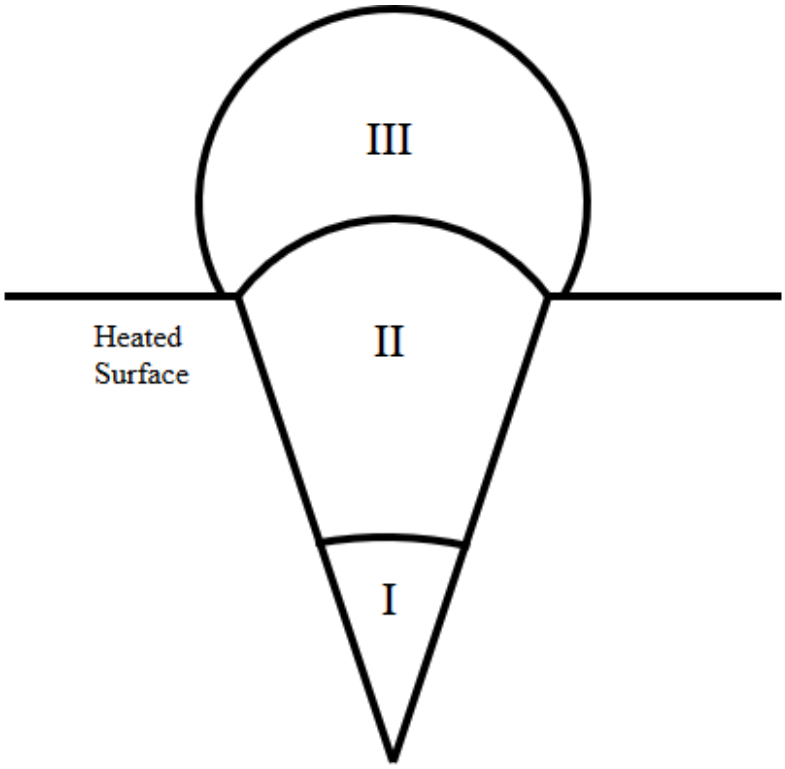


Figure 2.5: *Stages of bubble growth*

While bubbles appear to grow on flat surfaces, it is widely accepted that the majority of bubble inception occurs on microscopic cavities[7–9]. This is one of the primary reasons for the considerable uncertainty associated with bubble growth; boiling surface topology is difficult information to gather. A depiction of the stages of the bubble growth process is shown in Figure 2.5. Stage one begins the initial nucleation of the bubble. Stage two is when the bubble covers the mouth of the cavity while the last stage is when the bubble radius exceeds the mouth of the cavity. While this is seen as the typical bubble growth process of

a pure liquid, in the presence of dissolved salts, another nucleation site is possible. In the early stages of boiling of an electrolyte solution, it is possible that the dissolved salts which deposit on a heater surface may act as additional nucleation sites. The number of activity nucleation sites on a boiling surface is affected by the system pressure and wall temperature. As pressure is decreased in a system, more nucleation sites are available to produce bubbles. Additionally, as the wall temperature is increased, more sites are active and may produce bubbles.

The liquid near the wall of a boiling surface is superheated, meaning that the temperature of the liquid is higher than the saturation temperature. The thickness of the superheated liquid layer is dependent on the heat flux and the flow conditions of the fluid. For the same heat flux conditions, the temperature gradient is much steeper for flow boiling conditions compared to pool boiling. Additionally, the flow boiling is generally more turbulent then pool boiling under the same heat flux conditions. The superheated liquid layer increases vapor growth through evaporation at the liquid-vapor interface.

In a paper by Brooks et al.[10] the influence of subcooling and pressure on bubble diameter was seen for subcooled vertical annular flow boiling. It was suggested that at low pressure, the departure diameter is restricted as the bubble is unable to grow in the subcooled bulk fluid. The independence of subcooling suggests that at higher pressure, the bubble appears to depart before leaving the superheated liquid layer. The work performed in this report utilizes a low-pressure condition, so following the findings from Brooks et al. it may be expected that the bubble departure diameters is restricted and may be smaller due to the pressure condition. Additionally, the inclusion of salts will further compound this effect as dissolved salts inhibit coalescence and result in the development of smaller bubbles. Besides the work performed in this report, to the author's knowledge, there is currently one other literature report on the impact of dissolved salts in subcooled vertical boiling bubble departure diameter[11].

Bubble departure frequency is mainly seen as a function of bubble diameter, liquid subcooling, and wall heat flux[10]. A larger subcooling will lead to a decrease in bubble departure frequency. Since the fluid is further away from the saturation temperature, the bubble wait

Table 2.3: *Cation and Anion major constituents*[1]

Cations, Anions	**Seawater [mmol kg^{-1}]**
Na^{+}	470
Mg^{+2}	53
Cl^{-}	550
SO_4^{-2}	28

time is longer as it takes more time to heat the liquid back to a superheated condition. Additionally, a higher heat flux will lead to a higher departure frequency. The higher heat flux will increase the wall superheat and decrease the reheating time after a bubble departure. The impact of mass flow rate has little impact on the departure frequency[10].

For a vertical upward boiling flow scenario, there are several forces which contribute to bubble departure, such as contact pressure, buoyancy, hydrodynamic pressure, shear lift, growth, surface tension, and drag. At the point of bubble departure, several of these forces may be neglected. Following a model produced by Zeng and Klausner et al.[12] only the drag, buoyancy, and growth force should be considered in bubbled departure calculations. In forced convective boiling bubbles will often slide along the heated surface before departing. For vertical upward boiling flow, the bubble velocity should be faster than the fluid velocity causing the shear lift force to push the bubble against the heated wall. As the bubble slides along the heated surface, it will continue to grow. It will eventually depart after becoming large enough to merge with the two-phase mixture or through a transverse disturbance in flow[12].

The factors which contribute to bubble growth under a pure liquid scenario are altered in the case of seawater due to the presence of dissolved salts.

However, another critical factor which may contribute to bubble size is the number of available dissolved salts. A small list of the dominant ions in seawater is shown in Table 2.3.

It has been shown that while Na^{+} and Cl^{-} are the dominant ions[13], they do not have the most substantial influence on bubble formation diameter and coalescence. Ions such as Mg^{2+} and SO_4^{2-} play a more significant role in inhibiting coalescence in part due to the increased ionic strength of the ions. Lessard and Zieminiski[5] found that monovalent ions have less

of an effect compared to polyvalent ions in coalescence. The process of coalescence is still largely unknown. Currently, there is no widely accepted method for analytically predicting which ions will inhibit coalescence. An empirical method was developed by Craig et al.[14], which could predict the impact on the coalescence of several salts at concentrations up to 0.5M. However, at concentrations higher than 0.5M some of the salts in Craig et al. experiment, which was previously thought not to inhibit coalescence, did inhibit coalescence at concentrations higher than 0.5M. While there have been many studies on bubble production in electrolytic solutions with air as the gas, there have been very few studies with steam as the gas. The few available studies are most often involving a pool boiling scenario, which operates differently from the flow boiling scenario performed in this work.

There are many theories regarding the stability of bubble films in electrolyte solutions above the transition concentration. The transition concentration is the point at which bubble coalescence is significantly inhibited due to the electrolyte solution concentration. At seawater salt concentration, the popular DLVO theory is inaccurate[5;15;16]. Other popular bubble film stability models are centered around the van der Waals, electrostatic forces, ion-effect, Gibbs-Marangoni effect, and gas solubility[16].

Van der Waal attractions take place over a very short range of approximately 10 nm and less. This range is much shorter than the typical saline liquid film of gas bubbles. Therefore this cannot be used to explain the inhibition of coalescence of bubbles in artificial seawater. Another theory is the electrostatic double-layer (EDL), which assumes the negative charge on the surface of the bubbles prevents coalescence. In an experiment performed by Hsu et al.[17], it was suggested that the zeta-potential at quenching temperatures might increase EDL interactions. In that experiment, seawater was shown to quench at a significantly faster rate compared to water with little to no dissolved salts. However, the temperatures achieved in the experiment presented here are much lower than quenching temperatures and would not expect to impact the EDL interactions significantly. Additionally, EDL interactions are insignificant at concentrations higher than 0.01 M[16]. Another theory of bubble film stability is explained by the repulsive hydration pressure. The hydration pressure is thought to be caused by the closely bound first layer of water molecules on the air-liquid interface. The

tightly bound water molecules are expected to then prevent two bubble surfaces from approaching closer than 5-6 Å. However, the average rupture thickness is on the order of tens of nanometers. Therefore this effect does not appear to impact coalescence significantly. Another potential explanation is the hydrophobic interface of air-water. Through the addition of salts, the hydrophobic attraction is reduced and can lead to an increase in the inhibition of coalescence. The work performed in this study has vapor-water interaction as opposed to the widely investigated air-water interaction. The use of vapor-water interactions in electrolytic flow boiling has yet to be heavily investigated.

2.3 Electrolyte boiling review

There are many industrial and scientific processes which require the use of boiling of electrolyte solutions. A large portion of research in the boiling of electrolyte solutions revolves around the investigation of scale or fouling buildup. Scale or fouling is a process in which the dissolved solids in a solution precipitate out and become physically attached to the boiling surface. Scale or fouling is of particular interest due to a decrease in system efficiency and economic losses. An area in which electrolyte boiling is common is in thermal desalination processes. While boiling is a phenomenon which has yet to be resolved, the introduction of dissolved salts adds additional complexity to the analysis. Many of the literature experiments performed involve pool boiling as that is a common industrial process.

In a recent paper by Raghupathi and Kandlikar, seawater pool boiling fouling was characterized with respect to heat transfer and wall superheat[18]. In their paper, they stressed the importance of crystallization fouling plays in limiting the efficiency of thermal desalination. They reported that seawater resulted in a critical heat flux (CHF), which was much higher than that of deionized water. They proposed that this is due to the increase in nucleation site density, which is caused by scale formation. Additionally, they reported that the wall superheat was higher, which is also contributed to the scale build-up. The scale build-up led to an increase in thermal resistance and therefore, higher wall temperature. To prevent the higher wall superheat, they incorporated small metal beads which were physically lifted by

the boiling and then dropped on the boiling surface. This repeated contact of the metal balls lead to the smaller-scale formation and increased heat transfer rates compared to seawater boiling without the beads. Additionally, studies performed by Sarfaraz and Helali found that dissolved salts had a degrading effecting on the heat transfer rates[11;19].

In 2004, Jamialahmadi et al.[20] published results on their pool boiling electrolyte heat transfer experiments. Their results showed that at low heat fluxes bubble diameter increases, while the heat transfer rate decreases for an electrolytic solution relative to the distilled water. However, at higher heat fluxes, there was an increase in nucleation site density and decrease in bubble departure diameter, as well as an increase in heat transfer rate. Jamialahmadi et al.[20] developed a mass-diffusion based model to predict heat transfer rates in electrolyte solutions. Their model relied on the assumption that the increased salt concentration at the boiling surface was the dominant limiting factor in bubble departure size.

2.4 Natural circulation review

It is expected that the influence of dissolved salts would have an impact on the natural circulation flow rates. The presence of dissolved salts changes the density, viscosity, surface tension, and various thermodynamic properties, all of which would alter the expect flow behavior in a natural circulation loop. Two-phase natural circulation systems have been extensively researched due to their numerous industrial applications. The three most common areas of research involve applications in solar water heaters, electronic cooling, and nuclear power plant passive safety systems. Natural circulation systems are sought out due to their high heat transfer rate, ease of development, and passive operation. A variety of single and two-phase natural circulation loops have been constructed to study the impact of various heater and condenser orientations, and loop geometry on two-phase flow conditions[21–23]. This literature review will mainly consider the natural circulation loops which have a similar geometric orientation. There have already been many state-of-the-art reviews performed on natural circulation loops[24–26]. The orientation considered will be one in which the evaporator is near the bottom of one leg and the condenser on the top of the opposite leg. A depiction

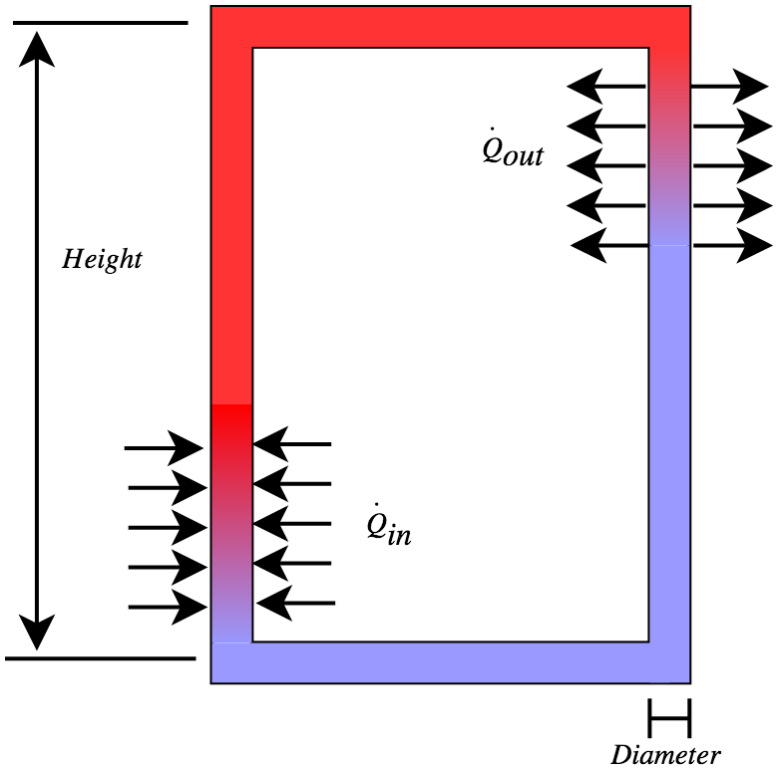


Figure 2.6: *Orientation of natural circulation loop*

of this orientation is shown in Figure 2.6. This orientation is also referred to as an HVCV or heated-vertically cooled-vertically.

Early thermal analysis on the stability of an HVCV natural circulation loop with similar dimensions was performed by Huang and Zelaya (1988)[27]. Their results showed that system efficiency could be improved by increasing the distance between the heater and condenser. However, this may introduce more instabilities, thereby decreasing efficiency. Kyung and Lee (1996)[28] were one of the first to attempt to connect heat flux, inlet subcooling, and restrictions with mass flow rate. They found that the maximum mass flow rate possible for any given heat flux was limited by the inlet subcooling. Further, they also found that at heat fluxes higher than that at the maximum flow rate caused boiling to become unstable and produced instabilities. In a single-phase experiment, Vijayan (2006) found that the HVCV orientation is the most stable configuration of natural circulation out of a combination of vertical and horizontal heater and condenser designs[29]. While there have been several studies on electrolytic pool boiling, to the author's knowledge, there is yet to be literature on the

impact of dissolved salts on two-phase natural circulation loops.

2.5 Flow Patterns

In two-phase flow, the distribution of the gas phase and liquid phase play an essential role in establishing the pressure drop and heat transfer rate characteristics. The influence of dissolved salts can alter the flow regime present through changes in hydrodynamic and thermal properties, most notably, density, surface tension, enthalpy, and latent heat of vaporization. Since dissolved salts change the overall density of the fluid, there may be a change in pressure drop. Additionally, the impact of inhibition of coalescence may shift the distribution of bubbles present towards smaller bubbles; however, the higher surface tension value of seawater suggests an increase in the production of larger bubbles. Each flow pattern can be categorized as one of several different types of flow regime. There are two basic categories of two-phase flow regimes which are dependent on the orientation of the flow with respect to the ground. The work performed in this study revolves around the use of vertically oriented flow, which is what will be covered in this chapter. In vertical upwards co-current two-phase flow the following flow regimes can be expected[6]; these patterns are also depicted in Figure 2.7:

1. **Bubbly flow** - In this regime, the gas is distributed in a way in which there are many discrete bubbles. The bubbles tend not to coalesce and remain much smaller than the diameter of the pipe. The general shape of the bubbles tends to very spherical while small and slightly non-spherical when larger. This regime is relatively stable with few oscillations. Additionally, this flow is highly homogeneous with mean properties consistent throughout the flow path. The dissolved salts within seawater inhibit coalescence; therefore, it would be expected that seawater in a two-phase flow loop would likely remain in the bubbly flow regime. However, this would compete with the higher surface tension value of seawater, which would suggest larger bubbles and more coalescence. If the inhibition of coalescence is dominant, then this would suggest the

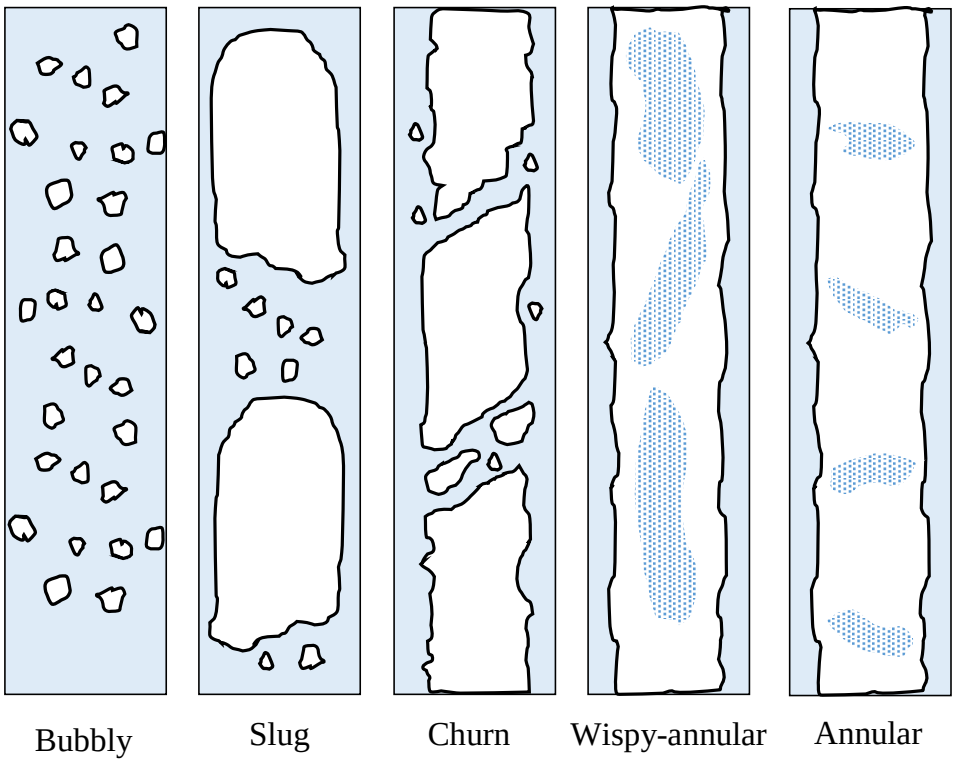


Figure 2.7: *Flow patterns in vertical co-current flow*

flow rate would be expected to be more stable than a pure water case.

2. **Slug flow** - Similar to the larger bubbles seen in the bubbly phase, this regime is dominated by bubbles that have a curved driving surface and flat tailing surface. A difference is that the bubbles in the slug regime are approximately the diameter of the pipe, while the bubbly regime is much smaller. Since these bubbles are slightly smaller than the diameter of the pipe, a thin liquid layer lies between the bubble and the pipe wall. This thin liquid layer tends to flow downward due to gravity while the bubble surrounding it flows upward. The formation of these bubbles is often the result of the coalescing of many bubbles. These bubbles are sometimes referred to as Taylor bubbles which derives its name from the Taylor instability. In between successive Taylor bubbles are liquid slugs, these slugs may contain smaller bubbles produced from the wake of the Taylor bubble. The wake of the Taylor bubble may incur significant form friction loss due to the fluid eddies produced by the large bubble. The length of these Taylor

bubbles can vary significantly depending on the flow conditions. The varying Taylor bubble lengths can cause significant variations in flow conditions such as flow rate and pressure. Slug flow has a higher deviation from single-phase flow behavior compared to bubbly flow due to the variability of slug flow bubble sizes.

3. **Churn flow** - This regime is characterized by having a higher vapor velocity than slug flow. The increasing velocity of the vapor creates a chaotic interaction between the gas and liquid phase. The liquid is predominantly on the channel walls while the vapor flows through the middle of the pipe channel. The falling liquid near the wall and the high vapor velocity produce shear stress in different directions on the fluid, causing a flow instability.

4. **Wispy-annular flow** - At even higher vapor velocities than churn flow, the shear stress begins to dominate the interaction between the gas and liquid phase. The increased shear stress leads to an annular ring of water to be formed inside the pipe channel. The middle of the pipe channel is filled with a mixture of high-velocity vapor and entrained water droplets.

In two-phase flow, it is possible for multiple regimes to exist locally within the same tube simultaneously. Take, for example, a uniformly heated vertical channel for which single-phase water enters the bottom. As the single-phase water travels upward, it heated until the saturation temperature is met. Along the surface of the heated wall, there is a developing thermal boundary layer. In this thermal boundary layer, the water can become superheated past the saturation temperature and can lead to nucleate boiling. Small vapor bubbles are generated on the surface, and as the water flows upward, the bulk fluid temperature approaches the saturation temperature. Since the bulk fluid temperature is higher at a higher position, the production of vapor increases, the increase in vapor generation causes more bubbles to be formed, which causes more coalescence. The coalescence causes large Taylor bubbles to form, which lead to slug flow. The slug flow then leads to annular flow. The annular ring of water seen in annular flow will eventually be heated past saturation temperatures and produce vapor. This leads to only single-phase vapor exiting the channel.

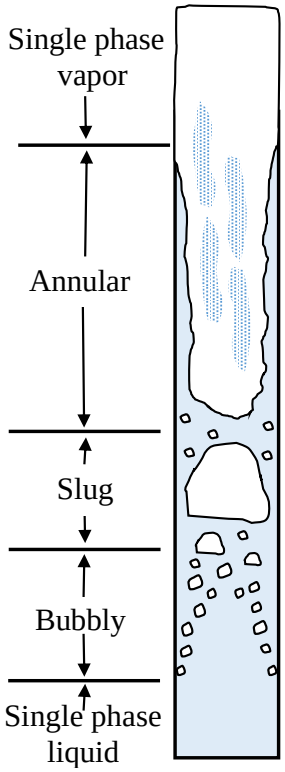


Figure 2.8: *Flow pattern development in heated vertical pipe*[6]

A depiction of this progression can be seen in Figure 2.8 The work presented here will have similar flow development to Figure 2.8.

2.6 Pressure Drop

An essential consideration in two-phase flow system design is the expected pressure drop. The pressure drop will determine the heat transfer and flow characteristics, which can affect the efficiency of the system. Given that the expected vapor production and flow regime may be different between seawater and freshwater case, it is expected that the pressure drop would then be influenced. The impact of dissolved salts change fluid properties in a minor way, but effect flow conditions majorly, this makes using conventional pressure drop models possibly unreliable. A few of the essential variables which are common in two-phase flow calculations will be discussed here. For future reference, the subscript "l" will be used to describe the liquid phase, while "g" will describe the gas phase. The first variable to be discussed is the

void fraction. The void fraction can be described in several ways, such as time-averaged, line-averaged, area-averaged, or volume-averaged. For this text, the area-averaged will be considered. "A" represented the cross-sectional area of the channel, while "A_g" represents the area in the channel occupied by the gas phase. A more detailed discussion of the void fraction will follow in Section 2.7.

$$\alpha = \frac{A_g}{A} \tag{2.6}$$

Another important variable is quality. The quality of flow describes the mass fraction of gas to liquid. A quality of zero represents no gas, while the quality of one represents only gas. Flow quality can be described by the following equation, where "$\dot{m}$" is mass flow rate. Additionally, mass flux is the mass flow rate per unit area.

$$x = \frac{\dot{m}_g}{\dot{m}_l + \dot{m}_g} \tag{2.7}$$

$$G = \frac{\dot{m}_{tot}}{A} \tag{2.8}$$

2.6.1 Homogeneous Flow Model

A common approach to two-phase pressure drop calculations is to treat both fluids as having the same flow velocities. This approach is generally considered applicable under flow scenarios such as bubbly or slug flow. Being as those flow regimes are most expected in a seawater case, it is likely that this model will be considered in later calculations. This model effectively considers the two phases to act as a single-phase having the mean properties of the two constituent phases.

The total pressure drop over a specific length can be calculated from the components of the pressure drop. The change in static pressure describes the pressure change due to elevation or height differences between the locations being measured. The momentum or acceleration pressure drop takes into consideration the acceleration of the vapor needed to

conserve the conservation of mass. Lastly, the frictional pressure drop is used to determine the pressure drop due to friction between the phases and the channel wall. The total pressure drop can then be calculated by taking the sum of each component of the pressure drop. This expression of the pressure drop gradient can be seen in Equation 2.9.

$$\left(\frac{dp}{dz}\right)_{total} = \left(\frac{dp}{dz}\right)_{static} + \left(\frac{dp}{dz}\right)_{momentum} + \left(\frac{dp}{dz}\right)_{friction} \tag{2.9}$$

The static pressure drop gradient can be calculated using the following equation:

$$\left(\frac{dp}{dz}\right)_{static} = \rho_H g \tag{2.10}$$

Where ρ_H is the homogeneous density, and g is the acceleration due to gravity. The homogeneous density can be calculated using equation 2.11. Using this equation, it can be seen that the expected static pressure drop would be larger for seawater than for freshwater since seawater has a higher density.

$$\rho_H = \rho_l \left(1 - \alpha\right) + \rho_g \alpha \tag{2.11}$$

In the previous equation $\rho_{l,g}$ denotes the respective liquid or gas phase density, while alpha represents the void fraction present.

$$\alpha = \frac{1}{\left(1 + \left(\frac{u_g}{u_l}\frac{(1-x)}{x}\frac{\rho_g}{\rho_l}\right)\right)} \tag{2.12}$$

The slip ratio of a flow can be described as the relative velocities of each phase in two-phase flow. For homogeneous flow, the phases are said to have equivalent velocities and therefore a slip ratio of one.

$$S = \frac{u_g}{u_l} \tag{2.13}$$

The momentum pressure drop gradient along the channel length is:

$$\left(\frac{dp}{dz}\right)_{momentum} = \frac{d(G^2/\rho_H)}{dz} \tag{2.14}$$

The frictional pressure drop gradient is found through the following equation:

$$\left(\frac{dp}{dz}\right)_{friction} = \frac{2f_{tp}G^2}{D\rho_H} \tag{2.15}$$

The two-phase friction factor f_{tp} can be found in a variety of ways. One method is to use the Blasius equation.

$$\frac{dp}{dz} = \frac{0.079}{Re^{0.25}} \tag{2.16}$$

Where μ_{tp} is the two-phase dynamic viscosity, which is a mass-averaged viscosity.

$$\mu_{tp} = x\mu_g + (1-x)\mu_l \tag{2.17}$$

The two-phase flow multiplier is the following[6]:

$$\Phi_{tp}^2 = \left[1 + x\left(\frac{(\rho_l - \rho_g)}{\rho_g}\right)\right]\left[1 + x\left(\frac{(\mu_l - \mu_g)}{\mu_g}\right)\right]^{-0.25} \tag{2.18}$$

2.6.2 Separated Flow Models

Unlike the homogeneous model, separated flow models consider the velocities of the phases to be different. This model is usually applied to two-phase in which there is a large relative velocity between the phases. Since seawater is expected to be seen in the bubbly regime, this may apply to the bubbly flow scenario. While the bubbly flow has a similar flow rate between phases, a significant bubble holdup may make this applicable. Bubble holdup is when the bubbles in the flow travel significantly slower than the water, creating a local increase in void fraction.

$$\triangle p_{total} = \triangle p_{static} + \triangle p_{momentum} + \triangle p_{friction} \tag{2.19}$$

The static pressure drop can be calculated similarly as the homogeneous static pressure drop. The main difference being the calculation of the density instead of using Equation 2.12 an expression developed by Rouhani and Axelsson (1970)[30] can be used. It should be noted that there are a variety of other methods available, but this one has been shown to have good agreement with experimental data.

$$\triangle p_{momenutm} = G^2 \left[\frac{x^2}{\rho_g \alpha} + \frac{(1-x)^2}{\rho_l (1-\alpha)} \right] \tag{2.20}$$

The frictional pressure drop is calculated in a similar way to the homogeneous method. However, the introduction of a two-phase multiplier is used. Two-phase multipliers are often used to correlate single-phase frictional pressure drop to two-phase frictional pressure drop. A variety of methods have been developed, and a few of those will be discussed here.

Friedel correlation (1979)[31]

This method also incorporates a two-phase multiplier.

$$\triangle p_{friction} = \Phi_{tp}^2 \triangle p_l \tag{2.21}$$

$$\Phi_{tp}^2 = E + \frac{3.24FH}{Fr_H^{0.045} We_l^{0.035}} \tag{2.22}$$

$$E = (1-x)^2 + x^2 \frac{\rho_l f_g}{\rho_g f_l} \tag{2.23}$$

$$F = x^{0.78}(1-x)^{0.224} \tag{2.24}$$

$$H = \left(\frac{\rho_l}{\rho_g} \right)^{0.91} \left(\frac{\mu_g}{\mu_l} \right)^{0.19} \left(1 - \frac{\mu_g}{\mu_l} \right)^{0.7} \tag{2.25}$$

The Weber number and Froude number are listed below. The Weber number is a ratio of the fluid's inertia to its surface tension. The Froude number gives the ratio of flow inertia to external field forces, in this case gravity.

$$We_l = \frac{G^2 D}{\sigma \rho_H} \tag{2.26}$$

$$Fr_H = \frac{G^2}{gD\rho_H^2} \tag{2.27}$$

$$\rho_H = \left(\frac{x}{\rho_g} + \frac{1-x}{\rho_l} \right)^{-1} \tag{2.28}$$

The inclusion of dissolved salts on two-phase natural circulation flow regimes has yet to be seen in the literature. There are, however, many reports on the impact of dissolved salts on bubble formulation. As discussed previously, salts tend to inhibit coalescence and therefore allow for many smaller bubbles. Smaller bubbles do not experience the same buoyancy force to drag force ratio as larger bubbles and therefore may move slower in the liquid relative to larger bubbles. This condition can create a separated flow in which the liquid may be moving faster than the bubbles. This can create high bubble hold up and increase void fraction locally. Separated flow models attempt to account for this difference by varying the weighting of the two-phase multiplier. The difference in hydrodynamic behavior between homogeneous and separated flow models is shown in Figure 2.9. The higher two-phase multiplier indicates that a highly separated flow would be expected to see a higher pressure drop than a homogeneous flow case. This, therefore, infers that the seawater natural circulation experiments will likely experience a more significant pressure drop over the test section.

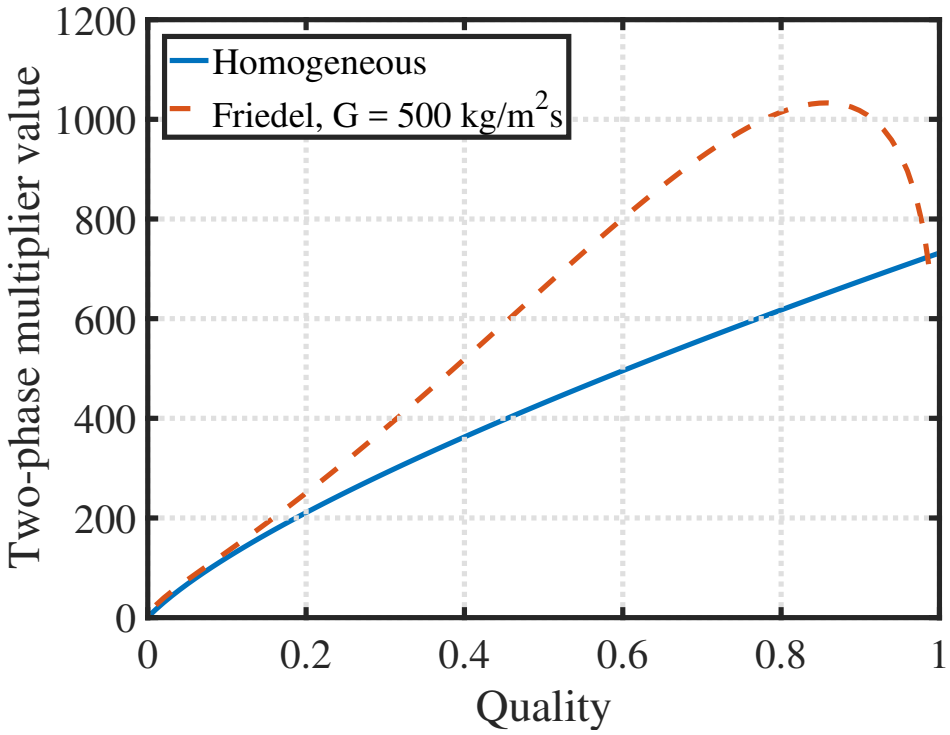


Figure 2.9: *Comparison of two-phase multipliers, properties taken at 101.325 kPa*

2.7 Void Fractions

There are a variety of geometric definitions which could be used to describe void fraction. The possible methods include line, cross-section, volume, and local. The line method is typically measured by passing a radioactive beam through a two-phase flow mixture and calibrating the beam based on the attenuation of the radiation. The resulting equation can be seen below:

$$\alpha = \frac{L_g}{L_g + L_l} \tag{2.29}$$

Where L_g is the length of the gas phase, and L_l is the length of the liquid phase.

A similar method can be performed for the cross-sectional area. Typical measurement devices include optical measurements or with the use of a conductivity mesh. The cross-sectional void fraction can then be described as follows:

$$\alpha = \frac{A_g}{A_g + A_l} \tag{2.30}$$

Note that this is the same as Equation 2.12. The A represents the area of each respective phase. Lastly, the void fraction can be measured using a volume-average method. In these cases fast acting valves can be used to stop flow and measure void fraction.

$$\alpha = \frac{V_g}{V_g + V_l} \tag{2.31}$$

In most cases, the cross-sectional void fraction calculation is used.

2.7.1 Homogeneous Flow

Void fraction using the homogeneous flow model can be calculated using Equations 2.12 and 2.13. The homogeneous model assumes that each phase is traveling at the same velocity. Therefore the slip ratio is equal to one. The only other considerations for the calculation of void fraction are the quality and relative densities between the liquid and gas phase. The bubbly flow regime is usually referred to as homogeneous flow given the similar flow rates experienced by both the vapor and liquid phase. Typically bubbly flow scenarios call for the use of homogeneous flow models for calculations of pressure and flow rate conditions.

2.7.2 Separated Flow

These methods consider that the velocities of each phase may not be the same. Many of the commonly used calculations involve empirical equations for specified operating ranges due to the high uncertainty involved in two-phase flow data. Flow regimes such as slug, churn, and annular are commonly used for this model. Given that bubbly flow is typically homogeneous and other regimes are separated flow, Figure 2.9 shows how the change in flow regime can impact of pressure drop in the system. The separated flow models account for a higher two-phase multiplier and therefore a higher pressure drop then homogeneous flow models.

Chapter 3

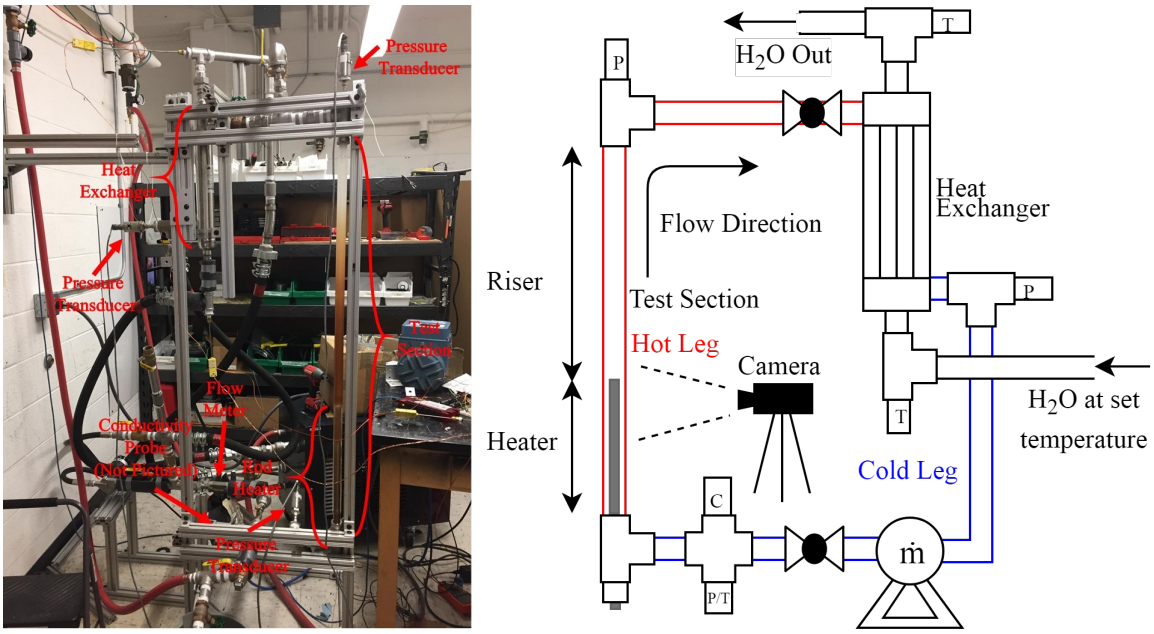
Experimental setup and operation

3.1 Setup

The experimental apparatus will be described in this section. Two-phase natural circulation experiments have been thoroughly investigated with a variety of fluids and loop characteristics. The following loop was designed to be similar to natural circulation loops seen in the literature. The system was designed to operate under 206.8 kPa gauge with various inlet conditions. The condition of 206.8 kPa gauge was selected to allow for optical transparent pipe for visualization of the flow regimes during experimentation. Most visually optical piping required a low operating pressure to incorporate it into the system. Additionally, measurement techniques and methods are described.

3.1.1 Heater

To heat the water to saturation and produce vapor, a heating element is needed. For this investigation, a commercial 2.7 kW rod heater was used. The heater had a diameter of 0.0158 m and a length of 0.61 m. The sheath material was Incoloy 800. 0.305 m lead wires were used to supply power to the heater. The heater had two sections which were not heated, the 0.0732 m by the incoming leads and 0.00635 m at the tip. Additionally, the heater was supplied with a type K thermocouple embedded at the end of the heater on the sheath. The



(a) Physical setup (b) Diagram

Figure 3.1: *Experimental setup*

location of the thermocouple is within in the unheated disc at the tip and therefore not a direct measurement of the heated wall surface temperature. However, the thermocouple is used as an estimation of the wall temperature at the tip of the heater.

3.1.2 Heat Exchanger

To reach a steady-state, the system needs to reject as much energy as being put into the system. To remove the heat supplied by the heater and condense the vapor a Shell and Tube heat exchanger was installed in the downcomer of the cold leg. The heat exchanger can also be referred to as a condenser. The heat exchanger has a relatively large heat transfer area of 0.251 m^2. The condenser ran in a counterflow manner in which the two-phase mixture entered the top and flowed to the bottom, while the cooling fluid entered from the bottom and exited at the top. The cooling fluid used on the secondary side was pressurized water supplied from a Delta T Systems temperature control unit. The coolant was set to a specific temperature, which resulted in a specific temperature at the inlet of the test section. The coolant ran at a flow rate of 1.26 liters/s. Type K thermocouples were added to the inlet and

outlet of the heat exchanger to observe changes in temperature of the coolant, and therefore find the heat rejection rate of the system. However, the flow rate used by the Delta T System was much too high in order to gather an accurate result.

3.1.3 Test Section

To view the behavior differences due to changes in salt concentrations and visual inspection of the flow was necessary. To facilitate inspection of the flow a 1.21 m long and 0.0254 m inner diameter borosilicate tube was used. This tube was fixed to the rest of the system piping through the use of Swagelok Ultratorr fittings. To allow the connection to the Ultratorr fittings, the ends of the glass piping were machined to an outside diameter of 0.0254 m. In the length of the pipe occupied by the internal heater, the effective hydraulic diameter was 0.0095 m.

3.1.4 Valves and Flow Channel

The piping throughout the system has a constant internal diameter of 0.0254 m everywhere except for a few valves and connections. The channel diameter is not 0.0254 m at the test section connections, condenser, and at the Emerson Coriolis flow meter. Two valves were added to the system to reduce flow oscillations and increase stability[32]. One of the valves is placed before the test section, and another is placed after the place section but before the heat exchanger. The control valve at the heat exchanger is a 0.0254 m inch globe valve set to a fixed position, while the other valve is a 0.00635 m needle valve which is fully open.

3.1.5 Measurement Devices

Shown in Figure 3.1 are the various letters which describe the instrumentation at that location. A "T" represents a type K thermocouple, a "C" represents an Emerson 4-electrode conductivity probe, while a "P" is for a pressure transducer. Attached to the Emerson conductivity probe is a PT1000 thermocouple which was used to measure the inlet test

section temperature. The conductivity probe was to monitor for an appreciable amount of deposition during the duration of the experiments. Lastly, the absolute pressure transducers were used to monitor the pressure drop across the test section and after the heat exchanger.

The error associated with each of the previously mentioned devices can be read in Table 3.1.

Table 3.1: *Instrumentation error*

Instrumentation	**Error**
Emerson Coriolis Flow Meter	±0.03 g/s
Emerson Conductivity Probe	±4% of reading
Type K Thermocouples	±2.2°C
Pressure Transducers (0-206.8 kPa abs.)	±0.4% FS
Variac Power Output	±30 W

3.2 Operation

The system was designed to be filled with water with three variations of salt concentrations. The first study was performed with deionized water, the next was with tap water, and the last was with deionized water mixed with artificial sea salt. The artificial sea salt used for simulating seawater was a commercially available product called *Instant Ocean*. This product is a good substitute for producing artificial seawater[1]. The major constituent ions from the artificial seawater compared to seawater can be seen in Table 3.2.

For each salt concentration case, water was first primed into the system, and then heating was allowed. The artificial seawater case required the water to be mixed before being placed into the system. Deionized water was thoroughly mixed with *Instant Ocean* at a concentra-

Table 3.2: *Cation and Anion concentration comparison of major constituents*[1]

Cations, Anions	**Seawater [mmol kg^{-1}]**	**Instant Ocean [mmol kg^{-1}]**
Na^{+}	470	462
Mg^{+2}	53	52
Cl^{-}	550	521
SO_4^{-2}	28	23

tion of 3.5% by weight. Once the system was filled, the heater was turned on under a low heat flux condition to allow for the water to reach the correct inlet temperature condition. The low heat flux prevented subcooled boiling and therefore premature salt deposition on the surface of the heater.

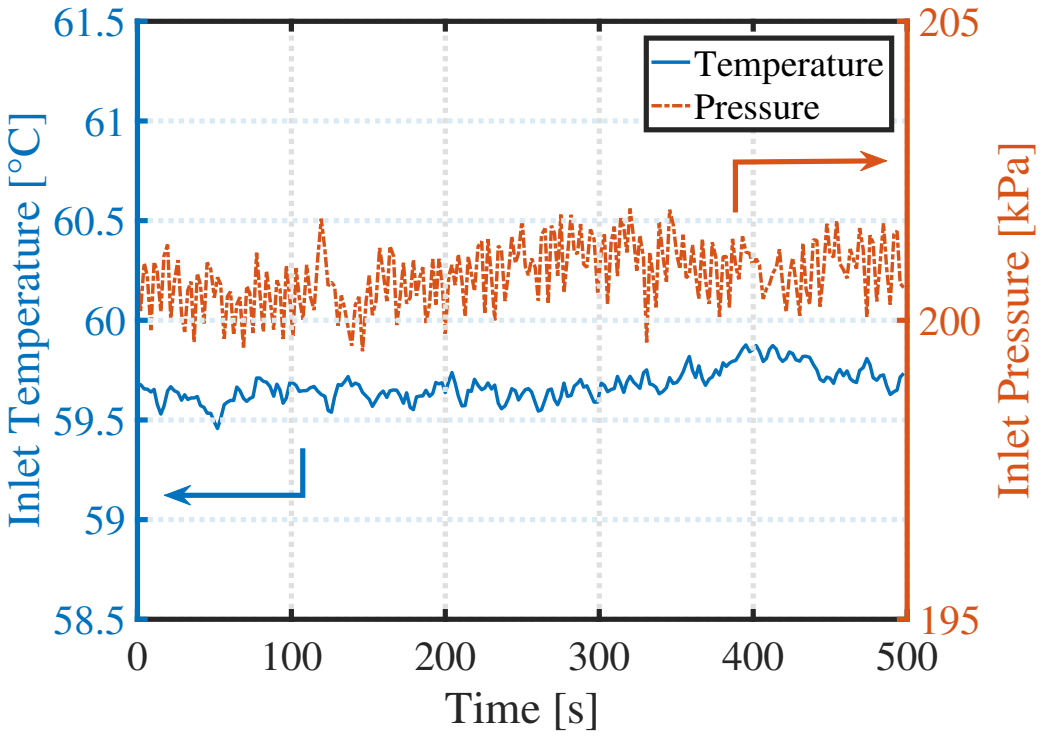


Figure 3.2: *Pressure and temperature at steady state conditions*

Once the correct inlet temperature condition was met, the heater power was then increased. The heater power was operated at specific powers between 1 kW and 2.7 kW. To ensure that the correct power was being supplied a variable transformer with a voltmeter was used. The voltages supplied were between 110 V to 180 V in increments of 10 V, with a heater rod resistance of 12 Ω. A voltmeter was attached to the heater circuitry to allow for constant monitoring of the power output with time. There was a minimal variation of the output voltage from the variable transformer. To allow for a consistent inlet temperature to the test section, the temperature on the secondary side of the heat exchanger was varied. On the secondary side of the heat exchanger was a water temperature control unit which allowed for the secondary side to be set at any temperature below 250 °F. At higher heater

powers, the temperature on the secondary side of the heat exchanger was lowered, and vise versa for lower heater powers.

The system ran at each power level until a steady-state condition had been met, starting from a low heat flux to a high heat flux condition. The criterion for a steady-state condition was set to have fluctuations no larger than ± 6.89 kPa for the measured pressure and ± 1.5 °C for the inlet temperature in 10 minutes. Figure 3.2 shows an example of what conditions were considered to be in a steady-state. The values in the figure are representative of the typical steady-state results. It can be seen that the values of temperature and pressure usually have fluctuations less than 0.5 °C and 3.4 kPa, respectively.

Chapter 4

Results and Discussion

The two-phase natural circulation study was performed with the use of three different fluids of varying salt concentrations. The first case was with deionized water, tap water, and then deionized water mixed with artificial sea salts. The results discussed in this chapter look at the differences in flow characteristics due to salt concentrations. There are several important parameters, each with their impact on two-phase flow regime present. All of the experiments reported in this chapter were conducted at a test section inlet temperature of 60±1.5°C and a pressure of 200±6.5kPa absolute.

4.1 Mass Flow Oscillations

The steady-state mass flow rates were plotted against the power level for each fluid. A view of the steady-state condition mass flow rates can be seen in Figure 4.1. Every data point on the graph represents the time-averaged mass flow rate for 5 minutes of steady-state conditions. The error bars in Figure 4.1 represent a 95% confidence interval on the mean mass flow rate. The graph shows a clear linear trend in mass flow rates with heater power. The trend indicates that the flow is in the gravity dominated regime as opposed to the friction dominated regime[25]. In the gravity dominated regime, changes in flow are due to variations in the homogeneous density of the channel and therefore the static pressure seen

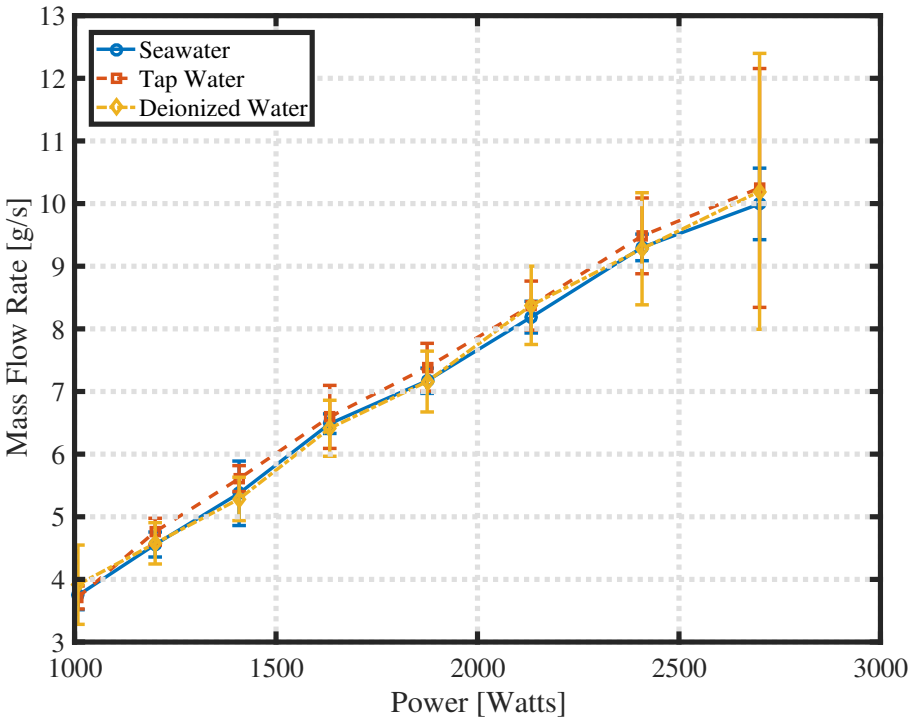


Figure 4.1: *Mass flow rate versus heater power at varying salt concentrations*

between the two legs. Another trend seen is the increase in the magnitude of the mass flow oscillations for the deionized and tap water cases as represented by the error bars. While the oscillations increase for the cases without sea salts, it is seen to only slightly increase for the seawater case. The cause for the increase in the magnitude of oscillations can be explained by the increase in heater power, which produces more vapor and moves the flow regime from bubbly to slug and churn. Both slug and churn have significantly more chaotic behavior as compared to bubbly flow. A clear depiction of the differences in mass flow rate oscillations can be seen in Figure 4.2. This figure shows the mass flow oscillations at 2.7 kW over approximately 250 seconds at a data collection rate of 0.5 Hz. At the 2.7 kW in Figure 4.1, the standard deviation from the mean flow values is approximately 5% for the seawater case, but up to 18-20% for the DI and tap water cases. Although, at the lower power level cases, the amplitude of flow fluctuations is very similar at approximately 5% of the mean flow rate. The stabilizing effect of seawater has been seen in isothermal two-phase bubble column experiments, previously reported in literature[33].

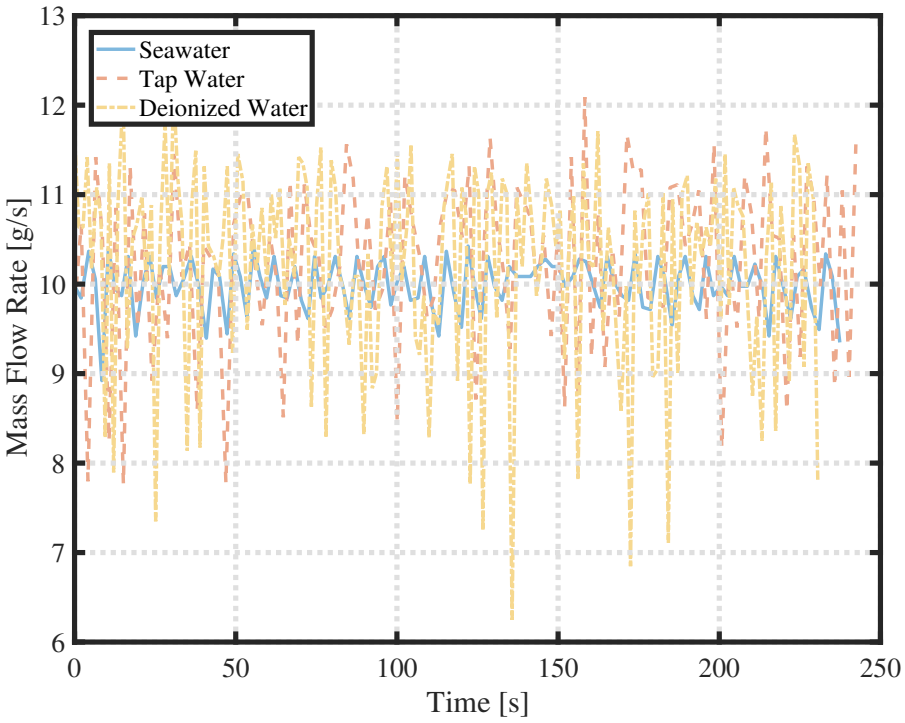


Figure 4.2: *Mass flow oscillations versus heater power at varying salt concentrations*

4.2 Monitoring dissolved salts

The electrical conductivity was monitored throughout the duration of the experiment to detected changes in dissolved salt concentrations. An electrical conductivity probe was placed before the inlet of the test section and monitored during the duration of the experiment. This monitoring probe can be used to infer the amount of salts deposited during the duration of the experiments. The experiments were run for approximately eight hours, which was not enough time for appreciable salt deposition. Shown in Figure 4.3 are the results of a single seawater test at various heater powers. It can be shown that resulting changes in electrical conductivity are minor and are well within the expected instrumentation error of 4% of the reading. Therefore, it can not be said that there was any appreciable amount of deposition which occurred throughout the eight-hour-long experiments. However, if the experiments were run for a longer time frame, it is expected that the deposition of salts would eventually become significant and thereby increase the wall heat transfer resistance

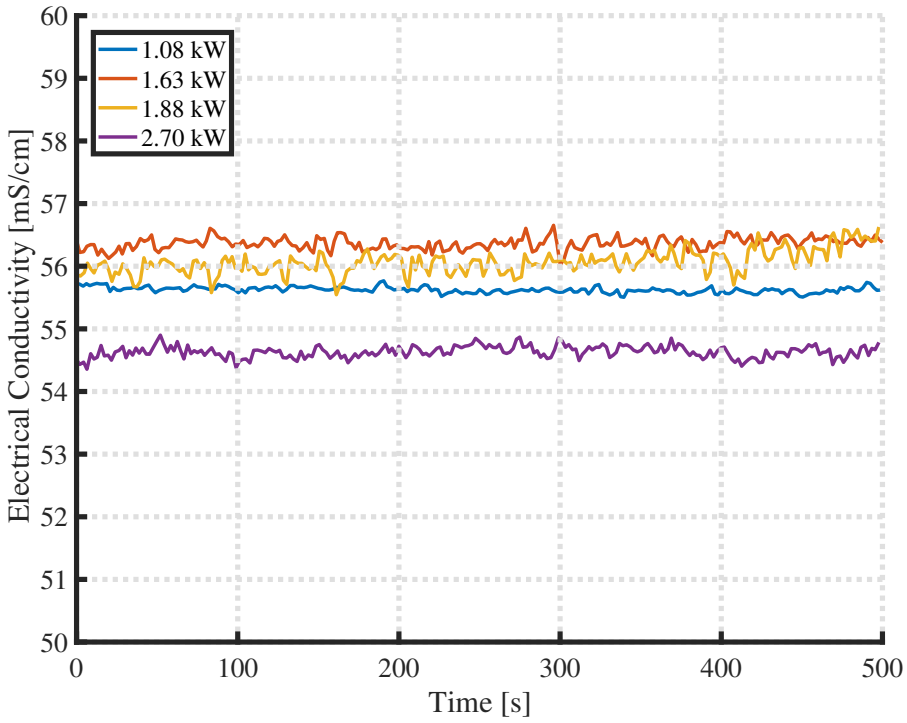


Figure 4.3: *Electrical conductivity with time*

Table 4.1: *Dissolved solids by electrical conductivity*

Salt Concentration	EC [μS/cm]	TDS[34] [mg/L]
Seawater	53760-58240	37632-40768
Tapwater	403.2-436.8	222-328
Deionized water	3.84-4.16	1.92-2.08

of the heater, leading to higher wall temperatures. The short time scale of the experiments and visual observations did not appear to show any substantial deposition.

The dissolved salts had the impact of increasing the saturation temperature, which also contributes to an increase in wall temperature. The bulk fluid boiling point elevation at seawater concentration equates to 0.585°C[2;3]. However, the impact of the boiling point elevation is expected to be increased as salts accumulate near-boiling surface due to bubble departure. As the vapor is generated on the heater surface, the superheated liquid layer around the bubble increases the local concentration of dissolved salts[18].

4.3 Bubble Dynamics

The driving force behind a two-phase natural circulation loop is the density differences between the hot and cold leg. That density difference creates a pressure difference between the two legs and causes for flow to occur. Therefore, the development of vapor generation and quality play an essential role in the formation of flow. At a higher quality, the homogeneous density will be less in the hot leg and will and cause an increase in the driving pressure.

Bubble growth and departure characteristics influence nucleate boiling. The diameter at which a vapor bubble leaves a heated surface is called the departure diameter. This parameter is vital when characterizing surface evaporative flux or nucleate boiling. By using bubble frequency, nucleate site density, and departure diameter estimates of evaporative flux can be evaluated. This is most relevant for coolants with dissolved salts as surface deposition sizes are dependent on bubble departure diameters[35–37].

The inclusion of salts prevent bubble coalescence and reduces bubble departure diameter. This is evident at the boiling surface of the rod heater, shown in Figure 4.4. The pictures are taken at a heater power of 1.2 kW. It is clear that the bubbles seen in the seawater case are significantly smaller than the tap water case. Additionally, the bubbles tend to be much more spherical than in the tap water case. The process of nucleate boiling is influenced by both bubble growth and departure. One possible conclusion for the reduction in bubble departure size is due to the supersaturation of the water by the dissolved salts. As a bubble begins to grow from a nucleation site, liquid water will vaporize into vapor. This process leaves behind the salts which were present in the liquid. Those dissolved salts then enter the superheated liquid layer at the base of the bubble. The supersaturation of salts increases the boiling point and decreases bubble growth period. This is shown in Figure 4.5. This could be seen as a diffusion-limited process due to the slow mass diffusion rates of the dissolved salts compared to thermal diffusion rates. The Lewis number, which is the ratio of mass diffusivity to thermal diffusivity, $Le = D_m/\alpha$, for seawater is 0.0125. A model was developed by Jamialahmadi et al.[20] in which a diffusion-based model is used to predict heat transfer rates in electrolyte pool boiling solutions. This has similarities to binary mixture boiling, in

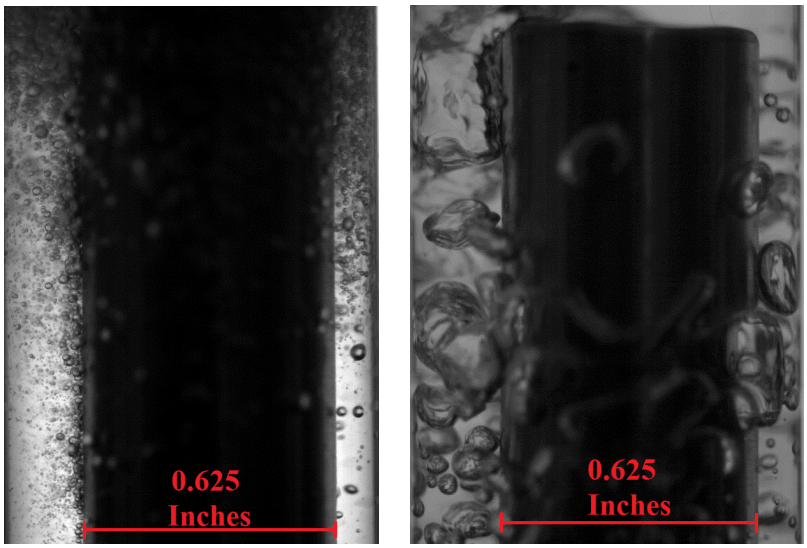


Figure 4.4: *Left: Seawater bubble formation at heater. Right: Tap water bubble formation at heater*

which is also considered a mass diffusion-limited process[38–40].

Another potential factor in the small bubble departure for the seawater case may be due to the surface wettability[41]. During the boiling of seawater, the dissolved salts present in the water can deposit on the boiling surface. The deposition process can lead to a porous surface which can alter the bubble growth dynamics. It was shown by Kim et al.[42] that the scale build-up of nano-particles led to a decrease in the contact angle. By using the Fritz equation for departure diameter, it can be seen how the decrease in contact angle would reduce departure diameter.

$$D_d = 0.0208\theta\sqrt{\frac{\sigma}{g(\rho_f - \rho_g)}} \tag{4.1}$$

This equation shows the relationship between the bubble departure diameter and wettability ($D_b \propto \theta$). Wettability may be increased by the deposition of dissolved salts. The dissolved salts change the heater surface topology and then can reduce the contact of water. This effect has been observed with other nanoparticle structures on boiling surfaces[43]. An increase in wettability due to salts leads to a lower contact angle, which may play a part in the explanation for the smaller departure diameters. High wettability has been shown to be able to increase the critical heat flux (CHF) of boiling systems by up to two times the

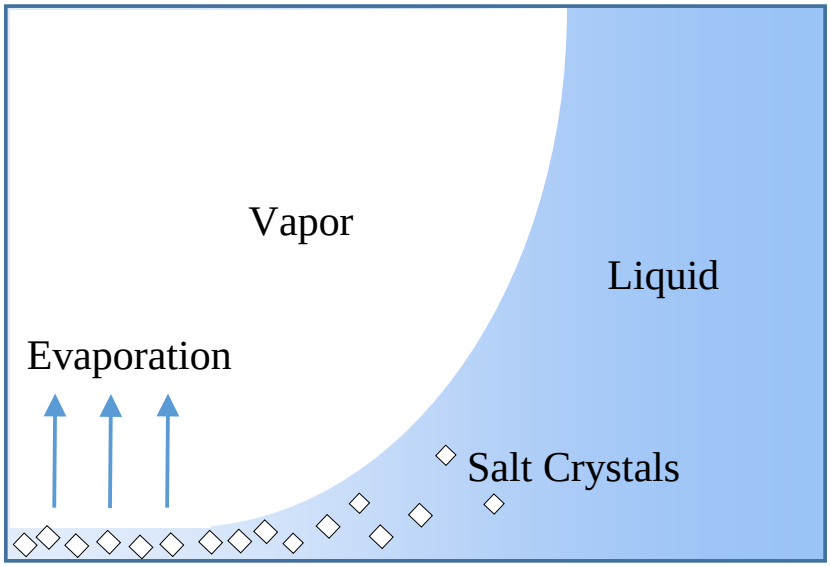


Figure 4.5: *Distribution of salt at bubble liquid-vapor interface*

normal value[42;44]. In their paper, Nam et al. found evidence that by increasing the surface wettability, the bubble departure diameter and growth period were reduced.

The tap water bubbles tend to continue to coalesce as they rise and form Taylor bubbles. The seawater bubbles do not coalesce in the riser section but do appear to grow slightly due to the decreasing static pressure at the higher elevations. The differences in bubble development in the riser section can be seen in Figure 4.6. The figure is also taken at the same heater power of 1.2 kW. Similar flow regimes are seen at 2.7 kW. The main difference for the deionized and tap water case is that the Taylor bubbles are significantly longer at the higher heater powers. In a recent paper by Wu et al.[45], it was proposed that at salt concentrations above the transition concentration, the transition from slug flow to bubble flow would be significantly delayed. Given that the artificial seawater was at concentrations higher than the transition concentration, Wu et al. appear to be correct in their prediction.

4.4 Pressure Drop

In the experimental setup were three pressure transducers. One was placed before the inlet of the test section, one at the top of the riser, and the last one at the exit of the heat exchanger.

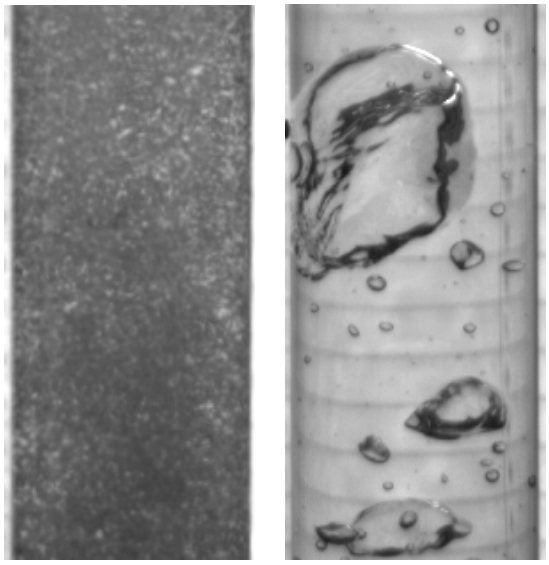


Figure 4.6: *Left: Seawater bubbles in riser section. Right: Tap water bubbles in riser section*

These pressure transducers were then used to monitor system pressure and then pressure drop across various points in the system. The placement of the pressure transducers can be seen in Figure 3.1. Pressure drop is a critical parameter which characterizes flow behavior and is important in the case of natural circulation. Shown in Figure 4.7 is the pressure drop across the test section. The error bars represent a 95% confidence interval on the mean absolute pressure. It should be noted that the pressure drop measurement is not across only the vertical channel. The pressure drop across the test section includes an elbow bend. The resulting pressure drop from this elbow bend is expected to be insignificant given the low flow velocity, and will not have an appreciable effect on the total pressure drop in the system.

It is clear that the deionized and tap water cases have very similar pressure drop across the test section. Overall, the seawater case shows a lower pressure drop over the entire range of heater powers. The pressure drop differences between seawater and deionized water increases, and heater power increases. Three factors which may contribute to the differences in pressure drop can be attributed to the difference in vapor generation and friction pressure drop and gas holdup. While the seawater needs less of an enthalpy rise to reach a saturation condition compared to the deionized and tap water cases, the lower mass flow rate of water in the seawater case makes it uncertain whether there would be an increase in vapor

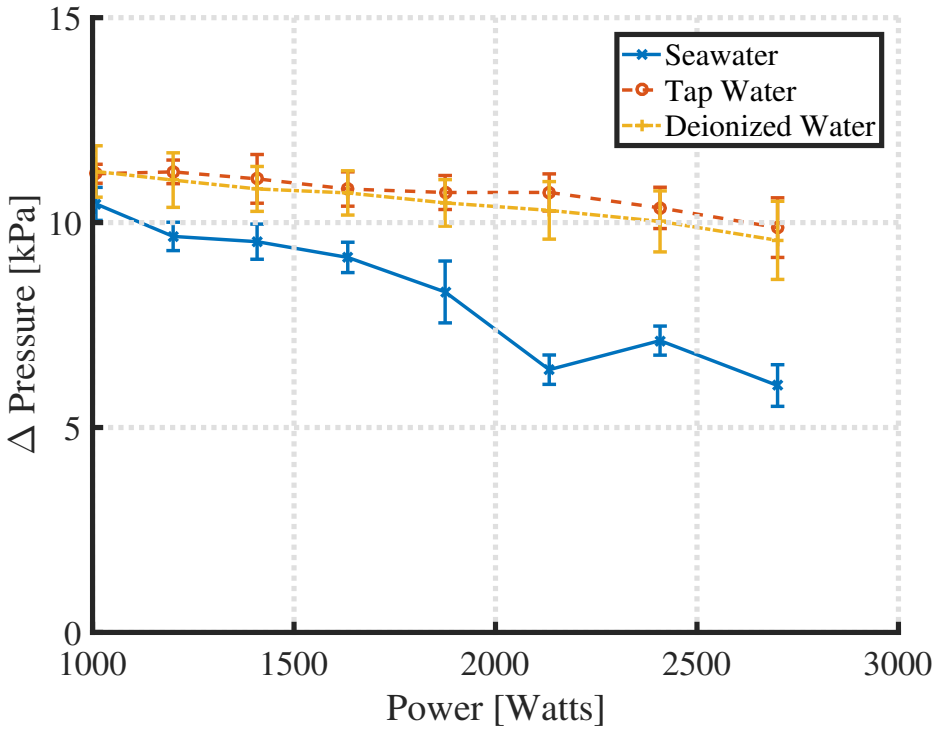


Figure 4.7: *Pressure drop over test section with heater power*

generation. This is shown in Equation 2.3 as a function of the Jakob number and latent heat of vaporization. The frictional losses in bubbly flow are different from that seen in slug flow. Slug flow has higher form friction, which would contribute to a higher pressure drop seen in the freshwater cases compared to the bubbly artificial seawater case. The two-phase multiplier for a range of models and flow regimes have been investigated in literature. It was found that the two-phase multiplier values for separated flow models are much larger than for homogeneous flow[46].

$$\Delta p_{fric} = \Delta p_l \Phi_{lo}^2 \tag{4.2}$$

Further, it may be possible that the vapor generation is very similar, but due to differences in vapor velocity between bubbly and slug flow, the gas holdup may be increased. An increased gas holdup would contribute to a lower pressure drop. More vapor in the hot leg would make the homogeneous density in that leg lower. A lower density in the hot leg

would mean that there would be a larger static pressure difference between the hot and cold legs. Therefore the change in pressure drop is primarily due to possible differences in vapor generation, frictional pressure drop, and gas holdup.

Chapter 5

Conclusions and Future Work

Two-phase natural circulation experiments were carried out with deionized water, tap water, and artificial seawater. The goal of this work was to investigate the impact of dissolved salts on steady-state natural circulation at different heat flux conditions. It was observed that under the same heat flux condition, each of the fluids showed similar average mass flow rates. However, the presence of dissolved salts had the impact of producing a stabilizing effect, which showed to reduce the overall magnitude of the mass flow oscillations seen. In large part, the stabilizing effect can be contributed to the dissolved salt's impact on both the bubble departure diameter and bubble coalescence. The salts majorly reduced the departure diameter seen on the boiling surface and significantly inhibited coalescence. The caused the flow regime for the artificial seawater case to be predominately in the bubbly regime. The bubble departure diameter was hypothesized to be influenced by an increase in wettability, which occurs due to scale formation on the heater surface. The increased wettability has been shown to produce bubbles of a shorter departure diameter. The effect of the dissolved salts on inhibiting coalescence is a topic of significant research today. While the exact cause of inhibiting coalescence is unknown, its impact was evident as the artificial seawater remained dominantly in the bubble flow regime while the freshwater cases were in the slug regime. The impact of the differences in flow regime was present in the increased pressure drop for the low dissolved salt concentration cases. The observations reported in this project provide

new insight into the potential use of seawater as a heat transfer process fluid in natural circulation loops for flow boiling applications.

Further investigation into this topic is needed to resolve the finer details of the operating differences between freshwater and seawater. This study was unable to quantify bubble departure diameter sizes due to not having access to photography capable of capturing such detail. Future work would involve the use of investigating more details of the bubble dynamics such as bubble departure size, bubble wait time, bubble growth time, etc. Additional useful results would include force convection results to view and major differences between natural circulation and forced convection operation. Further investigation is needed to better understand the efficacy of dissolved salts on stability, which could be performed with transient experiments. Longer operating times would be beneficial for allowing appreciable salt deposition amounts which could be measured by the electrical conductivity probe. Better instrumentation on the heater surface would provide more information about the wall temperature and relative differences between seawater and freshwater flow boiling operation.

Bibliography

[1] MJ J Atkinson, C Bingman, P O Box, C Bingman, and P O Box. Elemental composition of commercial seasalts. *Journal of Aquariculture and Aquatic Sciences*, VIII(2):39–43, 1997. ISSN 1939-3210. doi: 10.1080/19393210.2010.520340. URL http://www.rudyv.be/Aquarium/sels.pdf.

[2] Mostafa H. Sharqawy, John H. Lienhard, and Syed M. Zubair. Thermophysical properties of seawater : A review of existing correlations and data. *Desalination*, 16, 2013.

[3] Kishor G. Nayar, Mostafa H. Sharqawy, Leonardo D. Banchik, and John H. Lienhard. Thermophysical properties of seawater: A review and new correlations that include pressure dependence. *Desalination*, 390:1–24, 2016. ISSN 00119164. doi: 10.1016/j.desal.2016.02.024.

[4] Wolfgang Wagner and Hans-Joachim Kretzschmar. *International Steam Tables-Properties of Water and Steam based on the Industrial Formulation IAPWS-IF97: Tables, Algorithms, Diagrams, and CD-ROM Electronic Steam Tables-All of the equations of IAPWS-IF97 including a complete set of supplementary backward*. Springer Science & Business Media, 2007.

[5] Richard R. Lessard and Stefan A. Zieminski. Bubble Coalescence and Gas Transfer in Aqueous Electrolytic Solutions. *Industrial and Engineering Chemistry Fundamentals*, 10(2):260–269, 1971. ISSN 01964313. doi: 10.1021/i160038a012.

[6] John Collier and John Thome. *Convective Boiling and Condensation*. Clarendon Press, third edition, 1996.

[7] John D Bernardin and Issam Mudawar. A cavity activation and bubble growth model of

the leidenfrost point. *Transactions-American Society Of Mechanical Engineers Journal Of Heat Transfer*, 124(5):864–874, 2002.

[8] SF Jones, GM Evans, and KP Galvin. Bubble nucleation from gas cavitiesa review. *Advances in colloid and interface science*, 80(1):27–50, 1999.

[9] YY Hsu. On the size range of active nucleation cavities on a heating surface. *Journal of Heat Transfer*, 84(3):207–213, 1962.

[10] C.S. Brooks, N. Silin, T. Hibiki, and M. Ishii. Experimental investigation of bubble departure diameter and bubble departure frequency in subcooled flow boiling in a vertical annulus. *ASME 2013 Heat Transfer Summer Conf. Collocated with the ASME 2013 7th Int. Conf. on Energy Sustainability and the ASME 2013 11th Int. Conf. on Fuel Cell Science, Engineering and Technology, HT 2013*, 2:1–12, 2013. doi: 10.1115/HT2013-17308.

[11] Mohammad Mohsen Sarafraz and Faramarz Hormozi. Experimental studies o n the effect of water contaminants in convective boiling heat transfer. *Ain Shams Engineering Journal*, 5(2):553–568, 2014. ISSN 20904479. doi: 10.1016/j.asej.2013.11.006. URL http://dx.doi.org/10.1016/j.asej.2013.11.006.

[12] L. Z. Zeng, J. F. Klausner, and R. Mei. A unified model for the prediction of bubble detachment diameters in boiling systems- I. Pool boiling. *International Journal of Heat and Mass Transfer*, 36(9):2261–2270, 1993. ISSN 00179310. doi: 10.1016/S0017-9310(05)80111-5.

[13] David E. Slauenwhite and Bruce D. Johnson. Bubble shattering: Differences in bubble formation in fresh water and seawater. *Journal of Geophysical Research: Oceans*, 104 (C2):3265–3275, 1999. ISSN 01480227. doi: 10.1029/1998JC900064. URL http://doi.wiley.com/10.1029/1998JC900064.

[14] Vincent S.J. Craig, Barry W. Ninham, and Richard M. Pashley. The effect of electrolytes on bubble coalescence in water. *Journal of Physical Chemistry*, 97(39):10192–10197, 1993. ISSN 00223654. doi: 10.1021/j100141a047.

[15] M. Boström, D. R.M. Williams, and B. W. Ninham. Specific ion effects: Why DLVO theory fails for biology and colloid systems. *Physical Review Letters*, 87(16):1–168103, 2001. ISSN 00319007. doi: 10.1103/PhysRevLett.87.168103.

[16] Mahshid Firouzi, Tony Howes, and Anh V. Nguyen. A quantitative review of the transition salt concentration for inhibiting bubble coalescence. *Advances in Colloid and Interface Science*, 222:305–318, 2015. ISSN 00018686. doi: 10.1016/j.cis.2014.07.005. URL http://dx.doi.org/10.1016/j.cis.2014.07.005.

[17] Shu Han Hsu, Yuan Hong Ho, Ming Xi Ho, Jian Chiuan Wang, and Chin Pan. On the formation of vapor film during quenching in de-ionized water and elimination of film boiling during quenching in natural sea water. *International Journal of Heat and Mass Transfer*, 86:65–71, 2015. ISSN 00179310. doi: 10.1016/j.ijheatmasstransfer.2015.02.049. URL http://dx.doi.org/10.1016/j.ijheatmasstransfer.2015.02.049.

[18] Pruthvik A Raghupathi and Satish G Kandlikar. Preliminary results of pool boiling of seawater. pages 1–5. ASME Conference on Nanochannels, Microchannels, and Minichannels, 2017.

[19] A. B. Helali. Effects of water contamination on sub-cooled flow boiling heat transfer. *Energy Conversion and Management*, 52(5):2288–2295, 2011. ISSN 01968904. doi: 10.1016/j.enconman.2010.11.025. URL http://dx.doi.org/10.1016/j.enconman.2010.11.025.

[20] M. Jamialahmadi, A. Helalizadeh, and H. Müller-Steinhagen. Pool boiling heat transfer to electrolyte solutions. *International Journal of Heat and Mass Transfer*, 47(4):729–742, 2004. ISSN 00179310. doi: 10.1016/j.ijheatmasstransfer.2003.07.025.

[21] Daniel Gould, Daniel Franken, Hitesh Bindra, and Masahiro Kawaji. Transition from molecular diffusion to natural circulation mode air-ingress in high temperature helium loop. *Annals of Nuclear Energy*, 107:103–109, 2017.

[22] Daniel Franken, Daniel Gould, Prashant K Jain, and Hitesh Bindra. Numerical study of air ingress transition to natural circulation in a high temperature helium loop. *Annals of Nuclear Energy*, 111:371–378, 2018.

[23] Hitesh Bindra et al. Effects of modeling assumptions on the stability domain of bwrs. *Annals of Nuclear Energy*, 67:13–20, 2014.

[24] R Greif. Natural circulation loops. *Journal of Heat Transfer*, 110(4b):1243–1258, 1988.

[25] Alessandro Franco and Sauro Filippeschi. Closed loop two-phase thermosyphon of small dimensions: A review of the experimental results. *Microgravity Science and Technology*, 24(3):165–179, 2012. ISSN 09380108. doi: 10.1007/s12217-011-9281-6.

[26] Yoram Zvirin. A review of natural circulation loops in pressurized water reactors and other systems. *Nuclear Engineering and Design*, 67(2):203–225, 1982. ISSN 00295493. doi: 10.1016/0029-5493(82)90142-X.

[27] Bin-Juine Huang and R Zelaya. Stability Analysis of a Thermosyphon Loop. In *Advances In Solar Energy Technology*, pages 1091–1096. Elsevier, 1988.

[28] Ick Soo Kyung and Sang Yong Lee. Periodic flow excursion in an open two-phase natural circulation loop. *Nuclear Engineering and Design*, 162(2-3):233–244, 1996. ISSN 00295493. doi: 10.1016/0029-5493(95)01126-9. URL http://linkinghub.elsevier.com/retrieve/pii/0029549395011269.

[29] P. K. Vijayan, M. Sharma, and D. Saha. Steady state and stability characteristics of single-phase natural circulation in a rectangular loop with different heater and cooler orientations. *Experimental Thermal and Fluid Science*, 31(8):925–945, 2007. ISSN 08941777. doi: 10.1016/j.expthermflusci.2006.10.003.

[30] S Zia Rouhani and Eva Axelsson. Calculation of void volume fraction in the subcooled and quality boiling regions. *International Journal of Heat and Mass Transfer*, 13(2): 383–393, 1970.

[31] L Friedel. Improved friction pressure drop correlation for horizontal and vertical two-phase pipe flow. *Proc. of European Two-Phase Flow Group Meet., Ispra, Italy, 1979*, 1979.

[32] Long Sun Tong. *Boiling heat transfer and two-phase flow*. Routledge, 2018.

[33] Giorgio Besagni, Fabio Inzoli, Giorgia De Guido, and Laura Annamaria Pellegrini. The dual effect of viscosity on bubble column hydrodynamics. *Chemical Engineering Science*, 158(June 2016):509–538, 2017. ISSN 00092509. doi: 10.1016/j.ces.2016.11.003. URL http://dx.doi.org/10.1016/j.ces.2016.11.003.

[34] Anna F. Rusydi. Correlation between conductivity and total dissolved solid in various type of water: A review. *IOP Conference Series: Earth and Environmental Science*, 118(1), 2018. ISSN 17551315. doi: 10.1088/1755-1315/118/1/012019.

[35] NB Hospeti and RB Mesler. Vaporization at the base of bubbles of different shape during nucleate boiling of water. *AIChE Journal*, 15(2):214–219, 1969.

[36] Hitesh Bindra and Barclay G Jones. Deposition of metallic colloids under sub-cooled nucleate boiling. *Colloids and Surfaces A: Physicochemical and Engineering Aspects*, 397:85–91, 2012.

[37] Hitesh Bindra. *Effect of boiling on deposition of metallic colloids*. PhD thesis, University of Illinois at Urbana-Champaign, 2010.

[38] Chang Cai, Hong Liu, Xi Xi, Ming Jia, and Hongchao Yin. Bubble growth model in uniformly superheated binary liquid mixture. *International Journal of Heat and Mass Transfer*, 127:629–638, 2018. ISSN 00179310. doi: 10.1016/j.ijheatmasstransfer.2018.07.084.

[39] S. G. Kandlikar. Boiling heat transfer with binary mictures: Part II - Flow boiling in plain tubes. *Journal of Heat Transfer*, 120(May 1998):388–394, 1998.

[40] S. G. Kandlikar. Boiling Heat Transfer With Binary Mixtures: Part IA Theoretical Model for Pool Boiling. *Journal of Heat Transfer*, 120(2):380, 1998. ISSN 00221481. doi: 10.1115/1.2824260.

[41] Daniel Franken, Zayed Ahmed, Seth Eckels, Steven Eckels, and Hitesh Bindra. Impact of dissolved salts on two-phase flow and boiling heat transfer in a natural circulation loop. *Chemical Engineering Science*, 2019.

[42] S. J. Kim, I. C. Bang, J. Buongiorno, and L. W. Hu. Effects of nanoparticle deposition on surface wettability influencing boiling heat transfer in nanofluids. *Applied Physics Letters*, 89(15), 2006. ISSN 00036951. doi: 10.1063/1.2360892.

[43] Seungjin Kim, Mohan S Yadav, Justin D Talley, Andrew Ireland, and Stephen M Bajorek. Separate effects experiments for air-ingress in helium filled vessel. *Experimental Thermal and Fluid Science*, 49:1–13, 2013.

[44] Y. Takata, S. Hidaka, J. M. Cao, T. Nakamura, H. Yamamoto, M. Masuda, and T. Ito. Effect of surface wettability on boiling and evaporation. *Energy*, 30(2-4 SPEC. ISS.): 209–220, 2005. ISSN 03605442. doi: 10.1016/j.energy.2004.05.004.

[45] Benjamin Wu, Mahshid Firouzi, Travis Mitchell, Thomas E. Rufford, Christopher Leonardi, and Brian Towler. A critical review of flow maps for gas-liquid flows in vertical pipes and annuli. *Chemical Engineering Journal*, 326:350–377, 2017. ISSN 13858947. doi: 10.1016/j.cej.2017.05.135. URL http://dx.doi.org/10.1016/j.cej.2017.05.135.

[46] P Vassallo and K Keller. Two-phase frictional pressure drop multipliers for suva r-134a flowing in a rectangular duct. doi: 10.2172/850141.

Appendix A

Experimental Setup

This picture was taken after a artificial seawater boiling experiment. The test section shown on the right has a brown to white color gradient from bottom to top, this gradient is caused by rust deposition on the surface of the test section. This picture was taken prior to finding a rust contamination from a prior experiment. Preceding experiments involved through cleaning of the piping system by circulation and acetone-water mixture for several hours and cleaning with a pipe brush. After cleaning the system of rust, the amount of rust generation which occurred during the experiment was significantly less than what is shown.

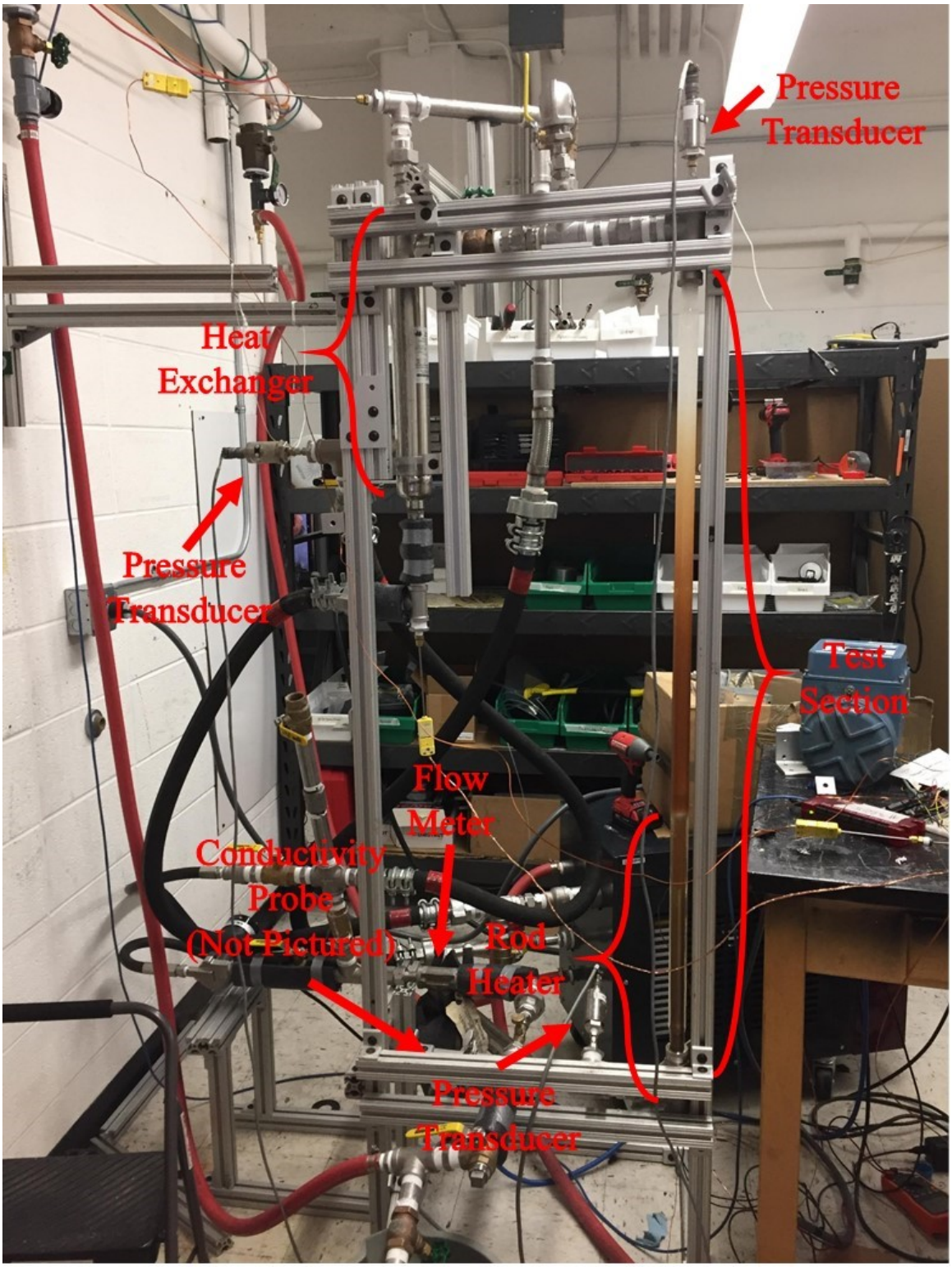


Figure A.1: *Experimental setup*

Appendix B

MATLAB Code

The following is code that was developed for use of data collection. This is the main file from which data was collected.

```
function stopping() %Main file
import Takedata
import DAQConfig
import Fix                  %Type "Fix" in the Command Window if stopping function errors out
import varcheck
handle = DAQConfig();
y = Takedata(handle);

%%%%%%%%%%%%%%%%%%%%%%%%%%%%%%%%%%%%%%%%%%%%%%%%%%%%CHANGE NAME TO MATCH EXPERIMENT%%%%%%%%%%%%%%%%%%%%%%%%%%%%%%%%%%%%%%%%%%%%%%%%%%%%
trial = 'Flow_Boiling_4'; %%KEEP FORMATTING I.E ('Trial_SubcooledTemp#C_Trial#')
%%%%%%%%%%%%%%%%%%%%%%%%%%%%%%%%%%%%%%%%%%%%%%%%%%%%CHANGE NAME TO MATCH EXPERIMENT%%%%%%%%%%%%%%%%%%%%%%%%%%%%%%%%%%%%%%%%%%%%%%%%%%%%
```

```
12
13 check = horzcat(trial,'.mat');
14 if exist(check)~=0
15     errmsg = input('MAKE SURE YOU ARE NOT OVERWRITTING DATA (LOOK
           AT LINE 10 & CURRENT FOLDER) (enter "y" if you think you
           are, or "n" if not):','s');
16     if errmsg =='y'
17         error('You may have successfully prevented data overwrite,
               congratulations')
18     end
19 end
20
21
22 %%
23 global KEY_IS_PRESSED %Global variable used to detect button press
24
25
26 KEY_IS_PRESSED = 0;
27
28 %%%%%%%%%%%%%%%%%%%%THESE LINES CREATE THE LIVE DATA PLOT
       %%%%%%%%%%%%%%%%%%
29 gcf;
30 h = gcf;
31 T1L = animatedline('Color','r');
32 T2L = animatedline('Color','r','LineStyle','--');
33 T3L = animatedline('Color','r','LineStyle',':');
34 T4L = animatedline('Color','k');
```

```
35 T5L = animatedline('Color','g');
36 C1L = animatedline('Color','c');
37 P1L = animatedline('Color','b');
38 P2L = animatedline('Color','b','LineStyle','--');
39 P3L = animatedline('Color','b','LineStyle','-.');
40 ML = animatedline('Color','m');
41 ax = gca;
42 ax.YGrid = 'on';
43 startTime = datetime('now');
44 set(gcf, 'KeyPressFcn', @myKeyPressFcn)
45 legend('TC1','TC2','TC3','TC4','TC5','C1L','P1','P2','P3','M','
     Location','northwest');
46 %%%%%%%%%%%%%%%%%%%%THESE LINES CREATE THE LIVE DATA PLOT
     %%%%%%%%%%%%%%%%%%
47
48 %%%%%%%%%%%%%%%%%%%%THESE LINES PLOT THE LIVE DATA
     %%%%%%%%%%%%%%%%%%%%%%%%
49 i = 0;
50 while ~KEY_IS_PRESSED
51         i = i + 1;
52         t =  datetime('now') - startTime;
53         addpoints(T1L,datenum(t),y(1))
54         addpoints(T2L,datenum(t),y(2))
55         addpoints(T3L,datenum(t),y(3))
56         addpoints(T4L,datenum(t),y(7))
57         addpoints(T5L,datenum(t),y(10)*8.475*6.25-25)% The 8.475
              converts the voltage to mA then from mA to a temp with a
```

```
    slope and offset from 0C to 100C
addpoints(C1L,datenum(t),y(11)*8.475*3.125+7.5)% Converts
    voltage to mA then converts mA to (mSiemen/cm) from 20 mS
    /cm to 70 mS/cm at the max
addpoints(P1L,datenum(t),y(4)*6)
addpoints(P2L,datenum(t),y(5)*6)
addpoints(P3L,datenum(t),y(6)*6)
addpoints(ML,datenum(t),y(9)/5.264) %Turns freqency to a
    mass flowrate (5.264Hz/(g/s))
ax.XLim = datenum([t-seconds(1200) t]);
datetick('x','keeplimits')

drawnow
%%
%%%%THIS SECTION OF CODE PRINTS OUT THE DATA TO THE CONSOLE
if i ==1 || mod(i,14)==0
    show1 = ['Time  |',' T1 |',' T2 |',' T3 |',' T4 |',' T5
        |',' C1  |','  P1 |','  P2 |','  P3 |',' M'];
    disp(show1);
end

show1 = [num2str(datenum(t)*24*3600,'%06.1f'),'|',num2str(y
    (1),'%#5.1f'),...
    '|',num2str(y(2),'%#5.1f'),'|',num2str(y(3),'%#5.1f'),'|
        '];
show2 = [num2str(y(7),'%#5.1f'),'|',num2str(y(10)
    *8.475*6.25-25,'%#5.1f'),'|',num2str(y(11)
```

```
            *8.475*3.125+7.5,'%#5.2f'),'|',...
77          num2str(y(4)*6,'%#5.2f'),'|',num2str(y(5)*6,'%#5.2f'),'|
                ',...
78          num2str(y(6)*6,'%#5.2f'),'|',num2str(y(9)/5.264,'%#5.3f'
                )];
79      show3 = horzcat(show1,show2);
80      disp(show3);
81      %%
82      %pause(0.5)
83
84      y = Takedata(handle); %%%GRABS THE DATA AND PUTS IT INTO
            VARIABLE Y
85  end
86  %%%%%%%%%%%%%%%%%%%%%%THESE LINES PLOT THE LIVE DATA
        %%%%%%%%%%%%%%%%%%%%%%%%
87
88  %%%%%%%%%%%%%%%%%%%%%%THESE LINES CLOSE OUT OF LABJACK
        %%%%%%%%%%%%%%%%%%%%%%%%
89  try
90      % Close handle
91      LabJack.LJM.Close(handle);
92  catch e
93      showErrorMessage(e)
94  end
95  %%%%%%%%%%%%%%%%%%%%%%THESE LINES CLOSE OUT OF LABJACK
        %%%%%%%%%%%%%%%%%%%%%%%%
96
```

```
97 %%%%%%%%%%%%%%%%%%%%THESE LINES SAVE DATA TO WORKSPACE
       %%%%%%%%%%%%%%%%%%%%
98 [timeLogs,tempLogs1] = getpoints(T1L);
99 [timeLogs,tempLogs2] = getpoints(T2L);
100 [timeLogs,tempLogs3] = getpoints(T3L);
101 [timeLogs,tempLogs4] = getpoints(T4L);
102 [timeLogs,tempLogs5] = getpoints(T5L);
103 [timeLogs,cLogs1] = getpoints(C1L);
104 [timeLogs,pLogs1] = getpoints(P1L);
105 [timeLogs,pLogs2] = getpoints(P2L);
106 [timeLogs,pLogs3] = getpoints(P3L);
107 [timeLogs,MLogs] = getpoints(ML);
108
109 assignin('base','time',timeLogs);
110 assignin('base','T1',tempLogs1);
111 assignin('base','T2',tempLogs2);
112 assignin('base','T3',tempLogs3);
113 assignin('base','T4',tempLogs4);
114 assignin('base','T5',tempLogs5);
115 assignin('base','C1',cLogs1);
116 assignin('base','P1',pLogs1);
117 assignin('base','P2',pLogs2);
118 assignin('base','P3',pLogs3);
119 assignin('base','M',MLogs);
120
121 T1 = tempLogs1;
122 T2 = tempLogs2;
```

```
123 T3 = tempLogs3;
124 T4 = tempLogs4;
125 T5 = tempLogs5;
126 C1 = cLogs1;
127 P1 = pLogs1;
128 P2 = pLogs2;
129 P3 = pLogs3;
130 M = MLogs;
131
132 timeSecs = (timeLogs-timeLogs(1))*24*3600;
133 assignin('base','timeSecs',timeSecs)
134
135 Data = horzcat(timeSecs.',T1.',T2.',T3.',T4.',T5.',C1.',P1.',P2.',
      P3.',M.'); %.' transposed the vector, horzcat concatenates to a
       single matrix
136 assignin('base',trial,Data);
137 %%%%%%%%%%%%%%%%%%%%THESE LINES SAVE DATA TO WORKSPACE
      %%%%%%%%%%%%%%%%%%%%
138
139 %%%%%%%%%%%%%%%%%%%%THESE LINES SAVE DATA TO WORKSPACE/ERROR CHECK
      %%%%%%%%%%%%%%%%%%%%
140 check = horzcat(trial,'.mat');
141 if exist(check)==0
142     newName = varcheck();
143     S.(newName) = Data;
144     save(trial, '-struct', 'S')
145 else
```

```
146     variableInfo = whos('-file',check);
147     newName = varcheck();
148
149     t = 1;
150     j = 0;
151     while t==1
152         for i=1:length(variableInfo)
153             if strcmp(newName,variableInfo(i,1).name)
154                 j = j+1;
155                 disp('Trial run has already been entered')
156                 newName = varcheck();
157             end
158         end
159         if j == 0
160             t = 0;
161         end
162         j = 0;
163     end
164     S.(newName) = Data;
165
166     if exist(check)>=1
167         save(trial, '-struct', 'S','-append')
168     else
169         save(trial, '-struct', 'S')
170     end
171 end
172 close all
```

```
%%%%%%%%%%%%%%%%%%%%THESE LINES SAVE DATA TO WORKSPACE/ERROR CHECK %%%%%%%%%%%%%%%%%%%%


function myKeyPressFcn(hObject, event)

global KEY_IS_PRESSED

KEY_IS_PRESSED  = 1;

disp('key is pressed')
```

This file was used to initialize the data acquisition system to allow for the correct reading of digital signals from instrumentation. The Labjack T7 Pro was used as the data acquistion system.

```
function y=Takedata(handle)

try


    %Setup and call eReadNames to read values.
    numFrames = 11;
    aNames = NET.createArray('System.String', numFrames);
    aNames(1) = 'AIN0_EF_READ_A';
    aNames(2) = 'AIN1_EF_READ_A';
    aNames(3) = 'AIN2_EF_READ_A';
    aNames(4) = 'AIN6';
    aNames(5) = 'AIN8';
```

```
14      aNames(6) = 'AIN10';
15      aNames(7) = 'AIN12_EF_READ_A';
16      aNames(8) = 'DIO0_EF_READ_A_F';
17      aNames(9) = 'DIO0_EF_READ_B_F';
18      aNames(10) = 'AIN4';
19      aNames(11) = 'AIN5';
20 %      aNames(4) = 'RTC_TIME_S';
21      aValues = NET.createArray('System.Double', numFrames);
22      LabJack.LJM.eReadNames(handle, numFrames, aNames, aValues, 0);
            %Reads values from Labjack
23
24      y=zeros(numFrames,1);
25      for i = 1:numFrames
26          y(i) = aValues(i); %Writes values to variable y
27      end
28
29 catch e
30      showErrorMessage(e)
31 end
32
33 end
```

This is the file which created an single object of all of the individual power levels for a given experiment.

```
1 classdef Temp2 < matlab.mixin.SetGet
2 %This is used to store runs as an object for easy use of grabbing
      contained.
3 %Used for 110V-190V in increments of 10V runs
```

```
4   properties
5       Value
6       Time
7       T1
8       T2
9       T3
10      T4
11      T5
12      Ts
13      T1S
14      T2S
15      T3S
16      T4S
17      T5S
18      C1
19      P1
20      P2
21      P3
22      Ps
23      M
24      Name
25  end
26  methods
27      function obj = Temp2(F)
28          %{
29          This is the constructor function used to create the
                intial
```

```
30          variables once the input matrix has been entered. It is
               important
31          that columns of the matrix follow the variable order
               below (i.e
32          first 5 columns=Thermocouple (TC) data, Conductivity,
               the next 3 = Pressure Transducer(PT) data and then
               Mass Flow rate)
33
34          %}
35          if nargin ~= 0
36              obj.Value = F;
37              obj.Time = F(:,1); %Time
38              obj.T1 = F(:,2);
39              obj.T2 = F(:,3);
40              obj.T3 = F(:,4);
41              obj.T4 = F(:,5);
42              obj.T5 = F(:,6);
43              obj.C1 = F(:,7);
44              obj.P1 = F(:,8);
45              obj.P2 = F(:,9);
46              obj.P3 = F(:,10);
47              obj.M = F(:,11);
48
49              obj.Ts = F(:,2:6);
50              obj.Ps = F(:,8:10);
51
52          end
```

```
53
54          m = size(obj.Time,1);
55
56          for i = 2:m %This for loop is used to convert the date/
                time column into seconds
57              if i == 2
58                  temp = obj.Time(i-1);
59              end
60              tdif = (obj.Time(i)-temp);
61              temp = obj.Time(i);
62              obj.Time(1) = 0;
63              obj.Time(i) = tdif+obj.Time(i-1);
64          end
65          m = length(obj.T1);
66          obj.T1S = zeros(m-2,1);
67          obj.T2S = zeros(m-2,1);
68          obj.T3S = zeros(m-2,1);
69          obj.T4S = zeros(m-2,1);
70          obj.T5S = zeros(m-2,1);
71          for i=1:m-2
72              if i == 1;
73                  obj.T1S(i,1) = obj.T1(i);
74                  obj.T2S(i,1) = obj.T2(i);
75                  obj.T3S(i,1) = obj.T3(i);
76                  obj.T4S(i,1) = obj.T4(i);
77                  obj.T5S(i,1) = obj.T5(i);
78              elseif i == 2
```

```
79                  obj.T1S(i) = mean(obj.T1(1:3));
80                  obj.T2S(i) = mean(obj.T2(1:3));
81                  obj.T3S(i) = mean(obj.T3(1:3));
82                  obj.T4S(i) = mean(obj.T4(1:3));
83                  obj.T5S(i) = mean(obj.T5(1:3));
84              else
85                  obj.T1S(i) = mean(obj.T1(i-2:i+2));
86                  obj.T2S(i) = mean(obj.T2(i-2:i+2));
87                  obj.T3S(i) = mean(obj.T3(i-2:i+2));
88                  obj.T4S(i) = mean(obj.T4(i-2:i+2));
89                  obj.T5S(i) = mean(obj.T5(i-2:i+2));
90              end
91          end
92      end
93      function r = temps(obj) %This function is used to plot the
            unfiltered thermocouple(TC) data
94          figure
95          num = 240;
96          r = plot(obj.Time(end-num:end)-obj.Time(end-num),obj.T5(
                end-num:end));
97          legend('T5');
98          set(findall(gca, 'Type', 'Line'),'LineWidth',2);
99          axes3=gca;
100         set(axes3,'FontName','Times New Roman','FontSize',28,'
                Layer','top','LineWidth',3);
101         xlabel('Time [s]')
102         ylabel('Temperature [C]')
```

```
103             grid on
104             g=gcf;
105         end
106         function r = smoothtemps(obj) %This function is used to plot
                the filtered TC data using a moving average
107             figure;
108             r = plot(obj.Time(1:length(obj.T1S)),obj.T1S,obj.Time(1:
                    length(obj.T1S)),obj.T2S,obj.Time(1:length(obj.T1S)),
                    obj.T3S,obj.Time(1:length(obj.T1S)),obj.T4S,obj.Time
                    (1:length(obj.T5S)),obj.T5S);
109             legend('T1','T2','T3','T4')
110             axes3=gca;
111             set(axes3,'FontName','Times New Roman','FontSize',28,'
                    Layer','top','LineWidth',3);
112             xlabel('Time [s]')
113             ylabel('Temperature [C]')
114             grid on
115             g=gcf;
116             g.Units='inches';
117             g.Position=[-19.9896 0.4271 12.7708 9.1875];
118         end
119         function r = press(obj) %This function plots the unfiltered
                Pressure Transducer data
120             figure
121             r = plot(obj.Time,obj.P1,obj.Time,obj.P2,obj.Time,obj.P3
                    );
122             legend('P1', 'P2', 'P3');
```

```
123         axes3=gca;
124         set(axes3,'FontName','Times New Roman','FontSize',28,'
                Layer','top','LineWidth',3);
125         xlabel('Time [s]')
126         ylabel('Temperature [C]')
127         grid on
128         g=gcf;
129     end
130     function r = mass(obj) %This function plots the filtered
            Mass Flow rate data using a moving average
131         figure;
132         m = length(obj.T1);
133         Mass = zeros(m-2,1);
134         for i=1:m-2
135             if i == 1;
136                 Mass(i,1) = obj.M(i);
137             elseif i == 2
138                 Mass(i) = mean(obj.M(i:3));
139             else
140                 Mass(i) = mean(obj.M(i-2:i+2));
141             end
142         end
143         r = plot(obj.Time(1:length(Mass)),Mass);
144         legend('M');
145         axes3=gca;
146         set(axes3,'FontName','Times New Roman','FontSize',28,'
                Layer','top','LineWidth',3);
```

```
147             xlabel('Time [s]');
148             ylabel('Mass Flow Rate [g/s]');
149             g=gcf;
150             g.Units='inches';
151             g.Position=[-19.9896 0.4271 12.7708 9.1875];
152         end
153     end
154 end
```